Scaling Breaking-Wave Vorticity Generation in the Surfzone

Bingchen Liu,[a] Falk Feddersen,[a] Sutara H. Suanda,[b] Matthew S. Spydell,[a] Mark A. Merrifield,[a]

[a] *Scripps Institution of Oceanography, University of California, San Diego, La Jolla, California, USA*

[b] *Department of Physics and Physical Oceanography, University of North Carolina Wilmington, Wilmington, North Carolina, USA*

Corresponding author: Falk Feddersen, ffeddersen@ucsd.edu

ABSTRACT: Spatially variable wave breaking generates vorticity in the surfzone, leading to transient rip currents (TRC), driving exchange between the surfzone and inner shelf. However, breaking-wave vorticity forcing is poorly understood, including its dependence on wave dissipation, directional spread, and beach slope. Using 72 Boussinesq model simulations on a planar beach, we examine the alongshore, cross- and time-lagged covariance of the vorticity forcing. The covariance is decomposed into separable functions, whose form and associated four dimensional parameters (forcing standard deviation $\hat{G}_0$, peak alongshore wavenumber $\hat{k}_{y0}$, propagation speed $\hat{c}$, and decorrelation time-scale $\hat{\tau}$) are derived from the simulations. The alongshore wavenumber spectrum is represented by a Weibull distribution. In a crest-following reference frame, the time-lagged covariance decays exponentially. The cross-crest lagged covariance changes sign as seen in example vorticity forcing. Nondimensional versions of $\hat{G}_0$ and $\hat{k}_{y0}$, depending on water depth, beach slope, and wave dissipation, scale well and increase with breakpoint wave directional spread $\sigma_{\theta b}$ up to 13.5°. The shallow water phase speed scales $\hat{c}$. Breakpoint significant wave height and gravity nondimensionalize $\hat{\tau}$, and the nondimensional $\hat{\tau}$ depends upon the normalized vorticity forcing magnitude $\hat{G}_0/\hat{G}_{\max}$. With focus upon covariance, we lose phase information on the alongshore wave-crest coherence. The simulations are limited in parameter space. We present a pathway for parameterizing vorticity forcing. As wave-averaged (WA) models do not include vorticity forcing, a parameterization could enable WA model study of interacting TRC and inner shelf processes over large regions.

SIGNIFICANCE STATEMENT: Rip currents are crucial for cross-shore exchange of larvae, pathogens, and sediment, thus playing a key role in human and ecosystem health. Breaking-wave generates vorticity in the surfzone, leading to transient rip currents (TRC). However, the breaking-wave vorticity forcing is poorly understood and is often not represented in models that span the surfzone and inner shelf. The purpose of this study is to better understand breaking-wave vorticity forcing. Our finding suggests that the forcing statistics can be predicted using beach slope, wave dissipation, and other bulk wave properties. The study points to a pathway towards a parameterization of breaking-wave vorticity forcing that could enable model study of interacting TRC and inner shelf processes over large regions.

1. Introduction

The surfzone is the nearshore region where depth-limited wave breaking occurs. Exchange of pollutants, larvae, and sediment across the surfzone is important for human health (*e.g.,* Boehm et al. 2015), ecosystem dynamics (*e.g.,* Morgan et al. 2018), and beach erosion (*e.g.,* Masselink et al. 2008). The surfzone is strongly stirred by horizontal eddies (vertical vorticity), particularly on alongshore uniform beaches (Spydell et al. 2007; Clark et al. 2010; Baker et al. 2021), driving exchange. Surfzone horizontal eddies are driven by finite-crest length wave breaking, generating vertical vorticity (Peregrine 1998; Clark et al. 2012), which then coalesce, likely due to inverse energy cascade (Spydell and Feddersen 2009; Elgar and Raubenheimer 2020; Elgar et al. 2023), leading to offshore-directed transient rip currents (TRC) offshore (Suanda and Feddersen 2015). On alongshore uniform beaches, TRCs are the principal mechanism of surfzone to inner-shelf exchange (Hally-Rosendahl et al. 2015; Suanda and Feddersen 2015; Hally-Rosendahl and Feddersen 2016; Kumar and Feddersen 2017a; Grimes et al. 2020; Grimes and Feddersen 2021).

The generation of surfzone vertical vorticity depends on along-crest gradients of energy dissipation on individual waves (Peregrine 1998). Thus, a model that resolves individual waves (wave-resolving, WR) is required to represent energy dissipation gradients. Boussinesq type (*e.g.,* depth-integrated) models are wave-resolving and can represent this vorticity generation mechanism (*e.g.,* Chen et al. 1999, 2003; Johnson and Pattiaratchi 2006; Spydell and Feddersen 2009; Feddersen 2014), which, on alongshore uniform beaches, depends critically on wave directional spread σ_θ (Spydell and Feddersen 2009; O'Dea et al. 2021; Nuss et al. 2025). Boussinesq models have been shown to reproduce low-frequency eddy statistics and the cross-shore structure of very low frequency rotational velocity observed in field (Feddersen et al. 2011) and laboratory (Nuss et al. 2025) settings suggesting the modeled vorticity generation mechanism is accurate. However, Boussinesq models are limited on the inner-shelf because they do not represent the vertical variation of circulation, density, and tracers. Reynolds-Averaged Navier–Stokes (RANS) type models (*e.g.,* CROCO, Treillou et al. 2025) are both depth-resolving and wave-resolving and can represent this vorticity generation mechanism (Marchesiello et al. 2021; Treillou et al. 2025). However, RANS type models are computationally expensive and are limited in the domain size.

Wave-averaged (WA) models have been widely used in a variety of nearshore applications (*e.g.,* Uchiyama et al. 2017; Wu et al. 2021, and many others). These models use a wave action equation to represent the effects of waves on circulation through radiation stress (Kumar et al. 2011) or the vortex force (Kumar et al. 2012). Although, these models can represent the effects of wave groups (Olabarrieta et al. 2023), they cannot represent the finite-crest length vorticity generation mechanism that leads to transient rip currents. However, WA models such as COAWST (Kumar et al. 2012) have the advantage of resolving the vertical and include density effects. This is important for examination of the effects of Stokes drift (Lentz et al. 2008) and winds (Lentz and Fewings 2012; Horwitz and Lentz 2014), important cross-inner shelf exchange mechanisms. As resolving individual waves is not required, the WA models can have much longer time-steps than WR models and are thus more computationally efficient. WA models have been used to simulate 30 km alongshore and 10 km cross-shore domains over months (Wu et al. 2020; Feddersen et al. 2021).

The effect of TRC on the inner shelf in both stratified and unstratified conditions is of particular interest, requiring a model that both resolves the vertical and resolves waves. One approach is to one-way couple a WR and a WA model, where the rotational component of the breaking-wave forcing (that generates vertical vorticity) is extracted from a WR model, and used as a time-dependent input body force in a WA model (Kumar and Feddersen 2017a). This approach results in similar WR (funwaveC) and WA (COAWST) model root-mean-square (rms) vorticity cross-shore profiles (Kumar and Feddersen 2017a) and has been used to study the effect of TRC on both the unstratified and stratified inner-shelf (Kumar and Feddersen 2017a,b,c; Grimes et al. 2020; Grimes and Feddersen 2021).

Yet, one-way coupling has significant disadvantages, requiring running both a WR and WA model for identical conditions and the laborious extraction of the rotational body force. Direct coupling is computationally inefficient. The WR model time-steps are on the order of $\Delta t = 10^{-2}$ s whereas WA time-steps are much larger ($O(1)$ s). Typical WR grid sizes are $\Delta x \approx 1$ m which limits the alongshore domain size to $O(1)$ km. In contrast, alongshore regions spanning 10 km or more are of interest in coupled surfzone/shelf modeling studies (*e.g.,* Kumar et al. 2015). A surfzone eddy generation parameterization for use with WA models would enable studies on inner-shelf effects of TRC relative to other realistic forcing mechanisms such as wind or internal tides.

Aside from increasing with wave directional spread σ_θ (O'Dea et al. 2021; Nuss et al. 2025), many details of breaking wave generated vorticity forcing are not well understood. Vorticity forcing is often associated with the ends of breaking-crests, the statistics of which have been studied in laboratory (Baker et al. 2023) and Boussinesq model (Nuss et al. 2025) contexts. Modeled vorticity forcing magnitude integrated over the surfzone has been shown to increase with σ_θ up to a maximum and subsequently decrease, likely due to a balance between larger total breaking-wave area at lower σ_θ and increased crest variability (crest ends) at high σ_θ (Nuss et al. 2025). Nuss et al. (2025) used a bulk approach, averaging over the surfzone or the breaking wave region. The statistics of vorticity forcing such as the alongshore scales, temporal, and cross-shore scales at a particular cross-shore location in the surfzone are not well understood. In particular, these statistics can have dependence on bathymetry and the incident wave field, quantities inherent to a WA model. If such statistics and their dependencies were known, then a parameterization of breaking wave vorticity forcing for a WA model could be developed.

Here, we examine the statistics of breaking wave vorticity forcing derived from a suite of 72 Boussinesq model simulations with a focus on the lagged covariance of vorticity forcing that depends upon the cross-shore coordinate and the alongshore-, cross-shore, and time lags. The model configuration, the suite of simulations, and examples of the vorticity forcing are described in Section 2. In Section 3a, the vorticity forcing covariance is defined and decomposed into separable functions that depend on the various lags. The form of these functions and their associated dimensional parameters are derived from the simulations. We then examine the alongshore wavenumber spectra of vorticity forcing in Section 3b and focus upon the time- and cross-shore lagged covariance in Section 3c. In Section 4, the key dimensional parameters estimated in Section

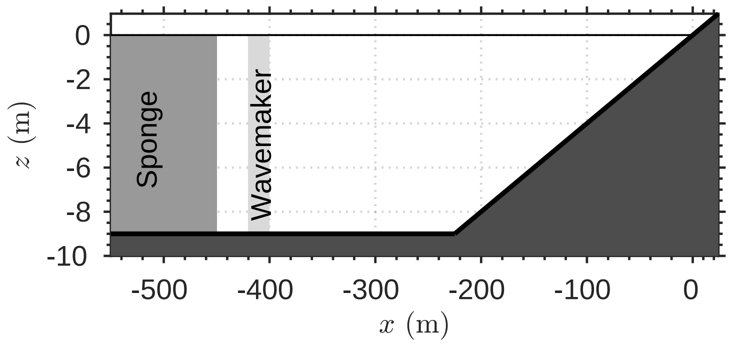

FIG. 1. funwaveC schematic showing model bathymetry $z = -h(x)$ versus cross-shore coordinate x, where $x = 0$ m is the still-water shoreline. The thin line at $z = 0$ m indicates the still water level. A wide sponge layer is located at the offshore end of the model domain (dark shaded region). A narrow (5 m) sponge layer is on the onshore end at the top of the beach (not indicated). The wavemaker (light shaded region) radiates waves onshore and offshore.

3 are nondimensionalized and scaled as a function of nondimensional parameters. A discussion of the implications of this study and a path to implementation of the parameterized breaking wave vorticity forcing follows in section 5.

2. Methods

a. funwaveC model and configuration

The open-source wave-resolving Boussinesq model funwaveC has been extensively used to study surfzone drifter and tracer dispersion, surfzone eddies, transient rip currents, and shoreline runup (*e.g.,* Spydell and Feddersen 2009; Feddersen et al. 2011; Clark et al. 2011; Guza and Feddersen 2012; Feddersen 2014; Suanda and Feddersen 2015; Hally-Rosendahl and Feddersen 2016). The time-dependent Nwogu (1993) model equations for horizontal velocity $\mathbf{u}$ and free-surface η are similar to the nonlinear shallow-water equations and include higher order dispersive terms, bottom and lateral friction, wave-generation, and breaking-wave forcing terms. Model details are found elsewhere (Feddersen et al. 2011; Suanda et al. 2016).

Germane to the topic of surfzone vorticity generation, the horizontal momentum equation for horizontal velocity $\mathbf{u}$ has schematic terms

$$\frac{\partial \mathbf{u}}{\partial t} + \ldots = \ldots + \mathbf{F}_{\mathrm{br}}\,, \tag{1}$$

where $\mathbf{F}_{\mathrm{br}}$ is the breaking-wave force represented as a Newtonian damping (Kennedy et al. 2000),

$$\mathbf{F}_{\mathrm{br}} = (h+\eta)^{-1}\boldsymbol{\nabla}\cdot[\nu_{\mathrm{br}}(h+\eta)\boldsymbol{\nabla}\mathbf{u}], \tag{2}$$

with the Lynett (2006) eddy viscosity ν_{br}, mean water depth h and the instantaneous free-surface elevation η. The $\mathbf{F}_{\mathrm{br}}$ has both an irrotational component that drives wave setup, and a rotation component ($\mathbf{F}_{\mathrm{br}}^{(\mathrm{rot})}$) that drives sheared surfzone alongshore currents and eddies. The generation of vertical vorticity ω can be written schematically as

$$\frac{\partial \omega}{\partial t} = \ldots + \nabla\times\mathbf{F}_{\mathrm{br}}, \tag{3}$$

where the dot product with the vertical unit vector $\hat{\mathbf{z}}$ is implied throughout on the right-hand-side. On an alongshore uniform bathymetry, non-zero $\nabla\times\mathbf{F}_{\mathrm{br}}$ is generated with finite-crest length breaking of a directionally spread wave field (Peregrine 1998; Spydell and Feddersen 2009; Clark et al. 2012).

The statistics of $\nabla\times\mathbf{F}_{\mathrm{br}}$ are examined with 72 idealized funwaveC model simulations that span wave and bathymetric slope properties (Suanda and Feddersen 2015). The bathymetry is alongshore uniform with alongshore domain length of 1200 m. The cross-shore domain length varies from 550 m to 784 m. The bathymetry has an offshore flat region (depth, $h = 9$ m) where waves are generated and a planar slope region extending above the mean water line allowing wave runup (Fig. 1). Grid resolution is 1 m in both cross (x) and alongshore (y) coordinates. The wavemaker (Suanda et al. 2016) generates directionally spread random waves from a Pierson-Moskovitz spectrum (Pierson and Moskowitz 1964) with a specific significant wave height H_{s} and peak period T_{p} and mean incidence angle $\bar{\theta} = 0°$. The normally incident waves have directional spread σ_θ (Kuik et al. 1988) with a Gaussian shape that is uniform at all frequencies. An offshore 100 m wide sponge layer absorbs the outgoing wave energy (Fig. 1). At the onshore boundary a 5-m wide sponge layer at the top of the beach is applied.

The 72 model simulations span a range of beach slopes ($\beta = 0.02, 0.03, 0.04$) and wave parameters: significant wave height ($H_\mathrm{s} = 0.5, 0.8, 1.1$ m), peak period ($T_\mathrm{p} = 8, 14$ s), and wave directional spread ($\sigma_\theta = 2.5°, 5°, 10°, 20°$). The peak period variation represents typical sea ($T_\mathrm{p} = 8$ s) and swell ($T_\mathrm{p} = 14$ s) cases. Simulations are run for 7800 s with output at 1 Hz. The last 4800 s is used for analysis once mean square vorticity has equilibrated (Feddersen 2014). Standard analyses (Kuik et al. 1988) are used to estimate $H_\mathrm{s}(x)$ and bulk $\sigma_\theta(x)$. The surfzone width L_SZ is defined as the distance from the shoreline to the x location where maximum significant wave H_s occurs. We define directional spread at $x = -L_\mathrm{SZ}$ as $\sigma_{\theta b}$. The Iribarren number at breaking $\mathrm{Ir_b}$, defined as

$$\mathrm{Ir_b} = \frac{\beta}{\sqrt{H_{s,\infty}/\lambda_b}}, \tag{4}$$

where $H_{s,\infty}$ is the deep water H_s and λ_b is the wavelength at $x = -L_\mathrm{SZ}$, varies from 0.13–0.44. Throughout, we define skill between two variables ϕ and ψ as $1 - \langle(\phi - \psi)^2\rangle/\mathrm{Var}(\phi)$ where Var represents the variance.

b. Example Model Simulation

An illustrative funwaveC simulation features incident random, directionally-spread waves that propagate shoreward, shoal, begin breaking near $x = -175$ m and dissipate as they approach the shoreline (Fig. 2). The model parameters here are $\beta = 0.02$, $H_\mathrm{s} = 1.1$ m, $T_\mathrm{p} = 8$ s, and $\sigma_\theta = 20°$. (horizontal dashed line in Fig. 2), and $L_\mathrm{SZ} = 172$ m in the example. Similar to previous wave-resolving simulations (*e.g.,* Spydell and Feddersen 2009; Feddersen et al. 2011; Feddersen 2014; Suanda and Feddersen 2015; Wei et al. 2017; Nuss et al. 2025), the directionally spread wave field results in finite crest length wave breaking generating a rich surfzone vorticity field with magnitude generally varying $\pm 0.1\ \mathrm{s^{-1}}$ that spans a range of scales (Fig. 2a). Seaward of the surfzone, vorticity is weaker and at larger length-scales.

We next examine vorticity forcing by the breaking waves. Within the surfzone ($x > -L_\mathrm{SZ}$), the curl of breaking wave forcing $\nabla \times \mathbf{F}_\mathrm{br}$ is non-zero in narrow cross-shore bands associated with the non-zero eddy viscosity due to wave breaking with magnitude generally varying $\pm 0.3\ \mathrm{s^{-2}}$ (Fig. 2b).

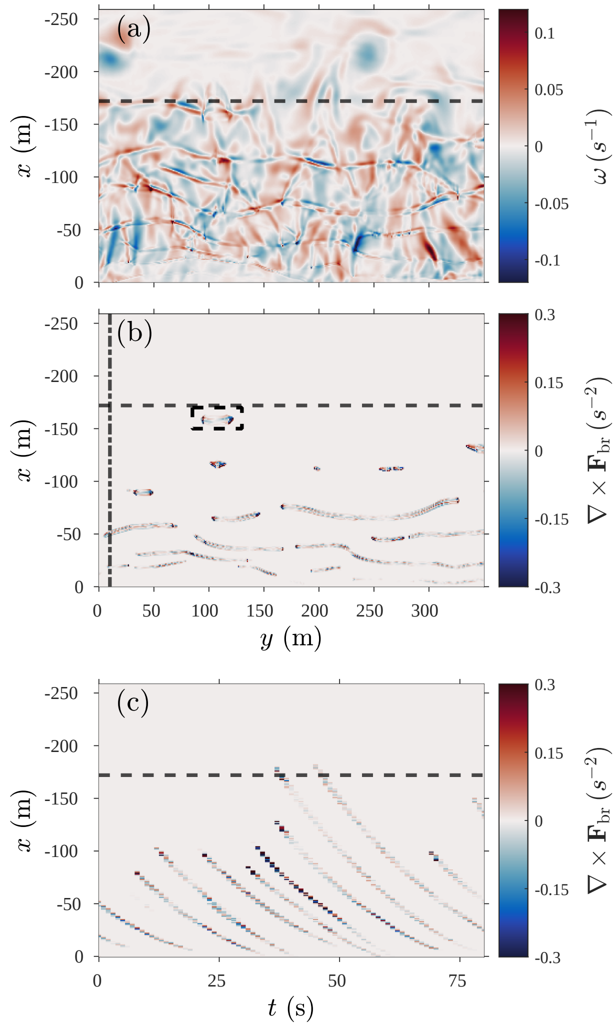

Fig. 2. Model snapshots of (a) vertical vorticity (ω) and (b) breaking-wave vorticity forcing ($\nabla\times\mathbf{F}_{\mathrm{br}}$) versus cross-shore ($x$) and alongshore ($y$) coordinates. (c) Hovmöller diagram of $\nabla\times\mathbf{F}_{\mathrm{br}}$ as a function of cross-shore (x) and time (t) at the cross-shore transect shown in vertical dash-dotted black line in panel b. Model parameters are beach slope $\beta = 0.02$ and incident wave parameters: $H_s = 1.1\,\mathrm{m}$, $T_p = 8\,\mathrm{s}$, and $\sigma_\theta = 20°$. The horizontal black dashed line indicates the outer limit of the surfzone $x = -L_{\mathrm{SZ}}$, where $L_{\mathrm{SZ}} = 172$ m. Dashed box in (b) highlights an individual breaking wave crest shown in Fig. 12.

This $\nabla\times\mathbf{F}_{\mathrm{br}}$ pattern is similar to models of a laboratory surfzone Nuss et al. (2025). The $\nabla\times\mathbf{F}_{\mathrm{br}}$ varies significantly in the cross-shore direction. In the outer surfzone ($x < -0.5\,L_{\mathrm{SZ}}$), wave breaking has just begun and the alongshore length of breaking wave crests are relatively short (Fig. 2b). In contrast, within the inner surfzone ($x > -0.5\,L_{\mathrm{SZ}}$), the length of breaking wave crests is longer as more of the wave crest has broken suggesting a larger net $\nabla\times\mathbf{F}_{\mathrm{br}}$. We next examine the time- and cross-shore variability of $\nabla\times\mathbf{F}_{\mathrm{br}}$ in (Fig. 2). Non-zero $\nabla\times\mathbf{F}_{\mathrm{br}}$ occurs in narrow cross-shore and temporal bands that propagate onshore with decreasing speed in shallower water (Fig. 2c). The occurrence frequency of non-zero $\nabla\times\mathbf{F}_{\mathrm{br}}$ bands is consistent with the model $T_{\mathrm{p}} = 8$ s. The $\nabla\times\mathbf{F}_{\mathrm{br}}$ bands begin generally between $x = -L_{\mathrm{SZ}}$ and $x = -(2/3)L_{\mathrm{SZ}}$ as not every random wave breaks at the same location. Within each band, $\nabla\times\mathbf{F}_{\mathrm{br}}$ varies relatively rapidly as the breaking wave crest propagates onshore.

We next highlight the effect of bathymetric slope and wave directional spread on the standard deviation of vorticity and vorticity forcing using simulations with the same incident H_{s} and T_{p} (Fig. 3). In all cases, H_{s} shoals to a maximum (defining L_{SZ}), slowly decreases in the outer surfzone and then rapidly decreases in the inner-surfzone (Fig. 3a,b). For fixed β, the cross-shore variation of H_{s} (and L_{SZ}) is essentially independent of σ_θ. Consistent with previous modeling studies (*e.g.,* Spydell and Feddersen 2009), the standard deviation of vorticity (std(ω)) is relatively weak seaward of the surfzone, increases onshore to a maximum in the inner-surfzone, decays towards the shoreline, and is stronger for increasing σ_θ up to 20° (Fig. 3c,d). The increase in std(ω) with σ_θ has also been observed in field studies (*e.g.,* Dooley et al. 2024). Onshore of $x = -L_{\mathrm{SZ}}$, the standard deviation of $\nabla\times\mathbf{F}_{\mathrm{br}}$ (std($\nabla\times\mathbf{F}_{\mathrm{br}}$)) increases rapidly to an inner-surfzone maximum (*e.g.,* Johnson and Pattiaratchi 2006), with a subsequent decay towards the shoreline (Fig. 3e,f). As with std(ω), std($\nabla\times\mathbf{F}_{\mathrm{br}}$) also is larger with increasing σ_θ which further emphasizes the explicit role of σ_θ in surfzone vorticity generation (Spydell and Feddersen 2009; Feddersen 2014; O'Dea et al. 2021; Nuss et al. 2025). Steeper bathymetry generally results in larger std($\nabla\times\mathbf{F}_{\mathrm{br}}$) and std($\omega$) (Fig. 3 left panels and right panels), likely due to the more intense wave dissipation with the larger β.

3. The covariance of vorticity forcing

a. Defining the covariance of vorticity forcing

To understand how the statistics of $\nabla\times\mathbf{F}_{\mathrm{br}}$ are affected by the incident wave field and the bathymetry, we focus upon the second order statistic of the lagged covariance of the breaking-wave vorticity forcing $\nabla\times\mathbf{F}_{\mathrm{br}}$. This covariance will be made up of separable functions (discussed below) that have key defining parameters that will be scaled by the wave and bathymetry statistics. For

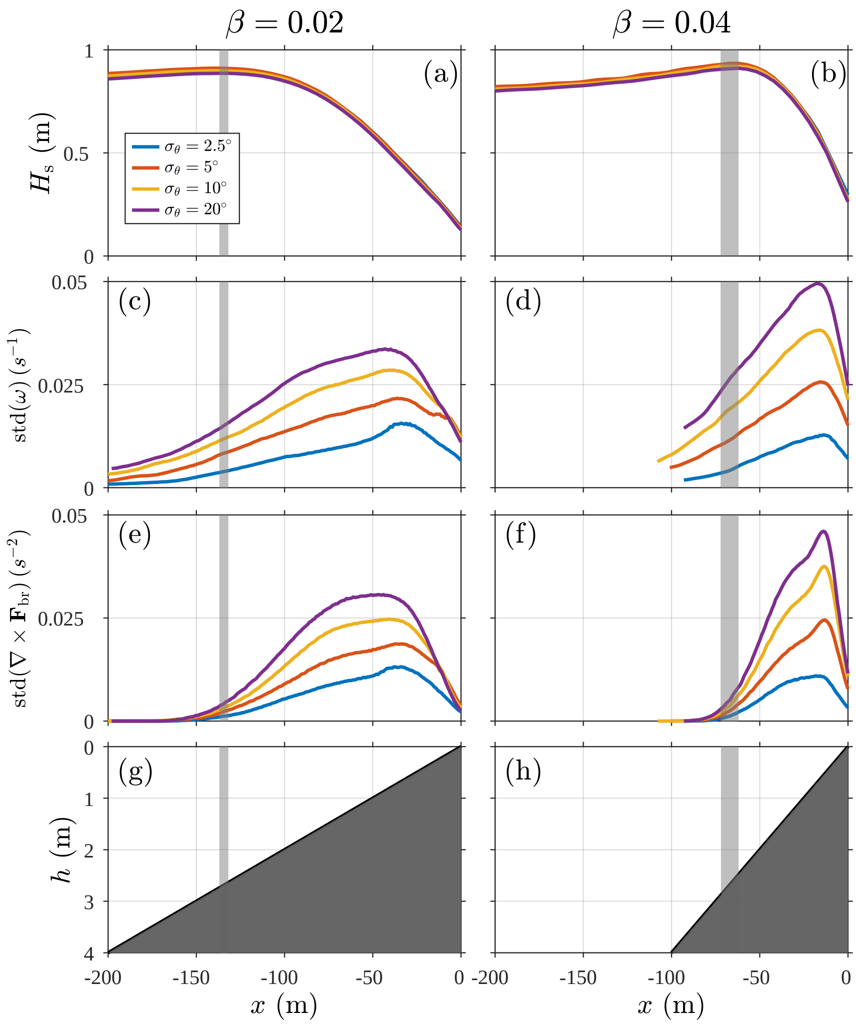

FIG. 3. Wave vorticity statistics and water depth versus cross-shore coordinate x: (a), (b) significant wave height H_s, (c), (d) standard deviation of vorticity std(ω), (e), (f) standard deviation of breaking-wave vorticity forcing std$(\nabla\times\mathbf{F}_{\rm br})$, and (g), (h) water depth h versus cross-shore coordinate x. All statistics are based on time and alongshore average. The bathymetry is alongshore uniform planar beach with slope of (left) $\beta = 0.02$ and of (right) $\beta = 0.04$. The shade region indicates $L_{\rm SZ}$ range for different simulations. Note, in (c)-(f), data were only stored out to 1.5 $L_{\rm SZ}$ and thus data farther offshore are not shown.

notational convenience, the vorticity forcing term is written as

$$G(x,y,t) = \nabla\times\mathbf{F}_{\rm br}. \tag{5}$$

Because the forcing is rotational, for mean normally-incident waves, the mean is zero, $\langle G\rangle = 0$ where $\langle\cdot\rangle$ indicates time and along-shore averaging. With the assumption that the statistics are stationary in time and in the alongshore (y), the space and time-lagged covariance of G is C_G

$$C_G(x,\Delta x,\Delta y,\Delta t) = \langle G(x,y,t)G(x+\Delta x,y+\Delta y,t+\Delta t)\rangle\,. \tag{6}$$

We now assume that the x, Δy, and $(\Delta x,\Delta t)$ dependence of C_G can be expressed as the product of separable functions of the form

$$C_G(x,\Delta x,\Delta y,\Delta t) = G_0(x)G_0(x+\Delta x)C_Y(\Delta y;x)C_{XT}(\Delta x,\Delta t;x), \tag{7}$$

where $G_0(x)$ is cross-shore dependent standard deviation of vorticity forcing magnitude ($G_0 = \langle G^2\rangle^{1/2}$), C_Y is the alongshore lagged (Δy) correlation, and C_{XT} is the time- (Δt) and cross-shore lagged (Δx) correlation. Note that $C_{XT} = 1$ at $\Delta x = 0$ and $\Delta t = 0$ and $C_Y = 1$ at $\Delta y = 0$. Next, a Fourier transform of C_G (7) in Δy yields

$$\mathcal{F}\left[C_G(x,\Delta x,\Delta y,\Delta t)\right] = G_0(x)G_0(x+\Delta x)S_Y(k_y;x)C_{XT}(\Delta x,\Delta t;x), \tag{8}$$

where k_y is the alongshore wavenumber and $S_Y(k_y)$ is the normalized alongshore wavenumber spectra of $\nabla\times\mathbf{F}_{\mathrm{br}}$ so that at all x,

$$\int S_Y(k_y)\,\mathrm{d}k_y = 1,$$

integrated over all k_y. Note with the above definition, the vorticity forcing alongshore wavenumber spectra is

$$S_{\nabla\times\mathbf{F}_{\mathrm{br}}}(k_y,x) = G_0^2(x)\,S_Y(k_y;x). \tag{9}$$

The function $C_{XT}(\Delta x,\Delta t;x)$ and $S_Y(k_y;x)$ will depend parametrically on quantities that depend on x such as water depth $h(x)$ or directional spread $\sigma_\theta(x)$, *e.g.,* $S_Y(k_y;\sigma_\theta(x),\ldots)$. These parametric dependencies will be derived from the modeled $\nabla\times\mathbf{F}_{\mathrm{br}}$.

b. Nondimensionalizing and fitting the alongshore wavenumber spectra of vorticity forcing

We now examine the alongshore wavenumber spectra $S_{\nabla\times\mathbf{F}_{\mathrm{br}}}(k_y)$, yielding insight into G_0 and S_Y (9). To estimate the alongshore wavenumber spectra at a cross-shore location, at each time step, $\nabla\times\mathbf{F}_{\mathrm{br}}$ is Fourier transformed in y and the $S_{\nabla\times\mathbf{F}_{\mathrm{br}}}$ is estimated by averaging the square Fourier transform magnitude over time. The fundamental wavenumber is $8.33 \times 10^{-4}\,\mathrm{m}^{-1}$ and the Nyquist wavenumber is 0.5 m^{-1}. The spectra is then interpolated on to a logarithmically-varying k_y, *i.e.*, $k_y \in [10^{-3.08}, 10^{-0.6}]\,\mathrm{m}^{-1}$, with a 0.001 increment in the exponent. The interpolated model spectra are then smoothed with a moving average, whose window length increases logarithmically with wavenumber, yielding $S_{\nabla\times\mathbf{F}_{\mathrm{br}}}(k_y)$. The variable window length increases degrees of freedom at large wavenumbers where the spectra can be noisy, yet preserves low wavenumber spectra shape. This interpolation and running average increases the smallest resolved k_y to 0.0017 m^{-1}.

The model $S_{\nabla\times\mathbf{F}_{\mathrm{br}}}(k_y)$ for all simulations and at five cross-shore locations ($x/L_{\mathrm{SZ}} \in [-0.75, -0.625, -0.5, -0.325, -0.25]$) are shown in (Fig. 4a). The $S_{\nabla\times\mathbf{F}_{\mathrm{br}}}$ peak magnitude spans three order of magnitude, indicating significant variation in forcing magnitude. The spectra levels are smaller in the outer surfzone and increase in the inner-surfzone (black to yellow in Fig. 4a), consistent with the variation of std($\nabla \times \mathbf{F}_{\mathrm{br}}$) (Fig. 3e,f). The spectra are relatively flat at low wavenumber and peak between 0.02 m^{-1} and 0.1 m^{-1}, with peak wavenumber k_{y0} that increases towards shore. This indicates that vorticity forcing alongshore length-scales vary with x. At higher wavenumber, the spectra decreases. The wavenumber dependence of $S_{\nabla\times\mathbf{F}_{\mathrm{br}}}$ at specific x-locations is similar to the surfzone-averaged $S_{\nabla\times\mathbf{F}_{\mathrm{br}}}$ from previous model studies on alongshore uniform bathymetries (Feddersen 2014; O'Dea et al. 2021).

A functional form that represents $S_{\nabla\times\mathbf{F}_{\mathrm{br}}}$ with a reduced number of parameters is needed to compactly describe $S_{\nabla\times\mathbf{F}_{\mathrm{br}}}$ and develop scalings for it. The model spectra resemble a Weibull distribution that is described with three parameters. Thus, at each cross-shore location (x), the alongshore wavenumber spectra are fit to a Weibull functional form of

$$S_{\mathrm{WB}}(x, k_y) = \hat{S}_0(x) \frac{\mu}{\lambda(x)^{\mu}} k_y^{\mu-1} \exp[-(k_y/\lambda(x))^{\mu}], \tag{10}$$

where $\hat{S}_0(x)$ and $\lambda(x)$ are fit-parameters. The parameter μ is fixed over all simulations and cross-shore locations, and is discussed below. Note with $\mu = 1$, the Weibull functional form in (10) becomes exponential distribution, and $\mu = 2$ corresponds to Rayleigh distribution. In addition, with an accurate fit, $\hat{S}_0 = G_0^2$ represents the variance of the vorticity forcing as by definition

$$\int_0^{\infty} \frac{\mu}{\lambda^{\mu}} k_y^{\mu-1} \exp[-(k_y/\lambda)^{\mu}]\, \mathrm{d}k_y = 1.$$

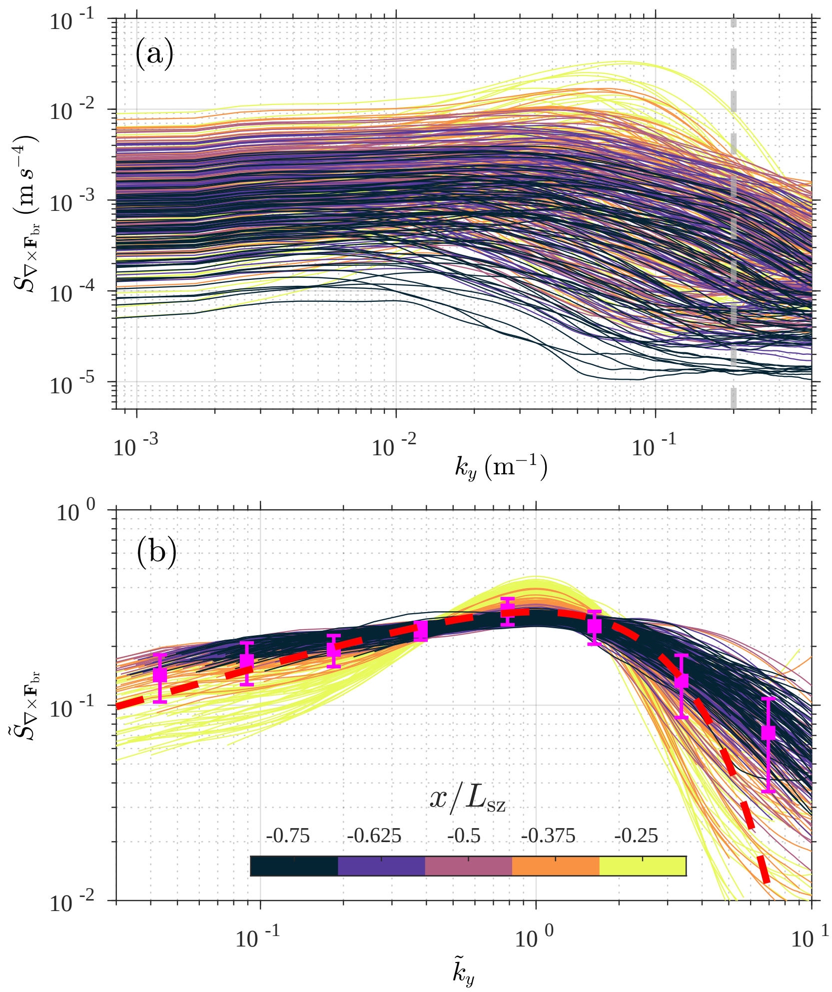

FIG. 4. (a) Alongshore wavenumber spectra of breaking-wave vorticity forcing $S_{\nabla\times\mathbf{F}_{\rm br}}$ versus alongshore wavenumber k_y at five different surfzone locations (colors) for all 72 model simulations. Vertical dashed line indicates spectra frequency cutoff of 0.2 m^{-1}. Color indicates cross-shore locations $x/L_{\rm SZ}$, where $L_{\rm SZ}$ is surfzone width. (b) Non-dimensional alongshore wavenumber spectra of vorticity forcing (17) versus non-dimensional alongshore wavenumber (16). Red dashed line indicates Weibull fit analytical expression (15). Magenta error bar indicates binned-mean and ± standard deviation of the spectra.

The peak wavenumber of the fit Weibull spectra ($\hat{k}_{y0}$) is

$$\hat{k}_{y0}(x) = \alpha\lambda(x). \tag{11}$$

where $\alpha = [(\mu-1)/\mu]^{1/\mu}$.

We choose the parameter μ by minimizing the the mean square error (MSE) between the model spectra and Weibull functional form as

$$\mathrm{MSE}(\mu) = \frac{1}{MN} \sum_{i=1}^{N} \sum_{j=1}^{M} \overline{(S_{\nabla\times\mathbf{F}_{\mathrm{br}},i,j} - S_{\mathrm{WB},i,j})^2}, \tag{12}$$

where i indicates simulations number (72 total) and j indicates one of five surfzone locations ($x/L_{\mathrm{SZ}} = \{-0.75, -0.625, -0.5, -0.375, -0.25\}$). Overline $\bar{\cdot}$ indicates a k_y average from 0.001–0.2 m^{-1}. The upper cutoff of 0.2 m^{-1} (indicated by the vertical dashed line in Fig. 4a) is chosen as we aim to represent well the vorticity forcing at scales greater than the water depth, which can be almost 3 m (Fig. 3g,h). The fits are performed over a range of μ from 1.1 to 1.7. We then estimate MSE(μ) (12), which is minimized with $\mu = 1.4$, representing a distribution between exponential and Rayleigh. Alternatively, the fit parameter μ could be a function of x. However, this would introduce additional and unnecessary complexity in the scalings.

The Weibull fit spectra in (10) can be non-dimensionalized using

$$\tilde{k}_y = k_y/\hat{k}_{y0} \tag{13}$$

$$\tilde{S}_{\mathrm{WB}} = \frac{S_{\mathrm{WB}}\,\hat{k}_{y0}}{\int_0^\infty S_{\mathrm{WB}}\,\mathrm{d}k_y}, \tag{14}$$

yielding a self-similar Weibull distribution:

$$\tilde{S}_{\mathrm{WB}} = \alpha\mu(\alpha\tilde{k}_y)^{\mu-1} \exp\left[-(\alpha\tilde{k}_y)^{\mu}\right]. \tag{15}$$

To evaluate the fit of the Weibull distribution to the model data spectra, the model spectra are non-dimensionalized similar to (13) and (14),

$$\tilde{k}_y = k_y/k_{y0}, \tag{16}$$

$$\tilde{S}_{\nabla\times\mathbf{F}_{\mathrm{br}}} = \frac{S_{\nabla\times\mathbf{F}_{\mathrm{br}}}\,\hat{k}_{y0}}{\int_0^\infty S_{\mathrm{WB}}\,\mathrm{d}k_y}, \tag{17}$$

where the model spectra peak wavenumber k_{y0} is used to normalize k_y (16) and the Weibull spectra (S_{WB}) and peak wavenumber ($\hat{k}_{y0}$) normalize the model spectra (17).

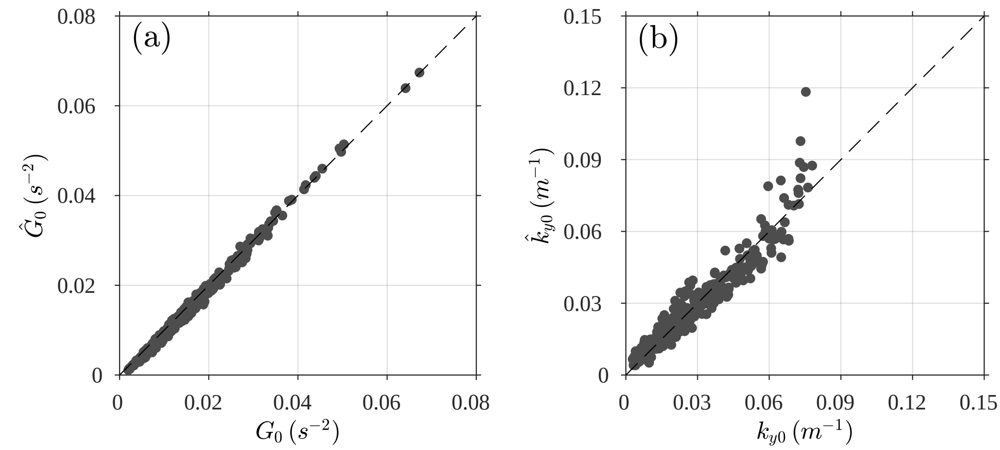

FIG. 5. (a) Integrated alongshore wavenumber spectra of Weibull fit $\hat{G}_0$ (18) versus integrated spectra of simulation G_0 (A1) in the same domain. Squared correlation r^2 between G_0 and $\hat{G}_0$ is $r^2 = 0.995$ and root-mean-square error of 0.001 s^{-2}. (b) Weibull fit spectra peak $\hat{k}_{y0}$ versus model spectra peak k_{y0}. Squared correlation r^2 between k_{y0} and $\hat{k}_{y0}$ is $r^2 = 0.92$ and root-mean-square error of 0.0054 m^{-1}. The dashed line represents the 1:1 relationship.

Across all simulations and all cross-shore locations, the non-dimensional $\tilde{S}_{\nabla\times\mathbf{F}_{\mathrm{br}}}$ largely collapse as a function of $\tilde{k}_y$ (Fig. 4b) with generally a factor of 2–3 variation for $\tilde{k}_y < 3$. This variation is far less than the 2 decade variation of $S_{\nabla\times\mathbf{F}_{\mathrm{br}}}$ for a particular k_y (Fig. 4a). The binned mean of $\tilde{S}_{\nabla\times\mathbf{F}_{\mathrm{br}}}$ follow closely the analytical Weibull distribution (compare magenta squares and dashed line in Fig. 4b) up to $\tilde{k}_y \approx 4$, well beyond the spectral peak. The standard deviation of the binned $\tilde{S}_{\nabla\times\mathbf{F}_{\mathrm{br}}}$ (vertical bars in Fig 4b) are small relative to the binned mean, further indicating that the $\tilde{S}_{\nabla\times\mathbf{F}_{\mathrm{br}}}$ is well represented by the Weibull distribution. At high wavenumbers $\tilde{k}_y > 4$, the Weibull distribution drops off faster than $\tilde{S}_{\nabla\times\mathbf{F}_{\mathrm{br}}}$. However, the variance contained at these high wavenumbers is generally low as shown in Appendix A. Within the inner surfzone (yellow in Fig. 4b), $\tilde{S}_{\nabla\times\mathbf{F}_{\mathrm{br}}}$ drops off faster in the high wavenumber compared to that in the outer surfzone (Black in Fig. 4b), Overall, this demonstrates that the Weibull distribution represents the overall $S_{\nabla\times\mathbf{F}_{\mathrm{br}}}(k_y)$ well with two parameters.

We next examine the Weibull distribution based fit parameters versus the spectral parameters. The Weibull distribution $\hat{G}_0$ is estimated as,

$$\hat{G}_0 = \sqrt{\int_{0.0017\,\mathrm{m}^{-1}}^{0.2\,\mathrm{m}^{-1}} S_{\mathrm{WB}}\,\mathrm{d}k_y}\ . \tag{18}$$

As we are interested in forcing length-scales significantly larger than the water depth, we restrict the integration to $k_y \le 0.2\ \mathrm{m}^{-1}$. We estimate G_0 over the same wavenumber limits which has a very small impact on G_0 (Appendix A). The model-derived forcing magnitude G_0 (A1) and fit-derived forcing magnitude $\hat{G}_0$ (18) and are highly correlated ($r^2 > 0.99$) with very small (0.001 s^{-2}) root-mean square errors (Fig. 5a). This demonstrates that the fit Weibull distribution represents well the magnitude of the vorticity forcing at scales appropriate for generating 2D turbulence. Next, the peak wavenumber (k_{y0}) of $S_{\nabla\times\mathbf{F}_{\mathrm{br}}}$ also compares well to that of the Weibull fit $\hat{k}_{y0}$ (Fig. 5b) with $r^2 = 0.92$ and root-mean-square error of 0.0054 m^{-1}. For the few $k_{y0} > 0.07\ \mathrm{m}^{-1}$ the $\hat{k}_{y0}$ overpredict k_{y0} by $\approx 33\%$. Note that all the $k_{y0} \le 0.08\ \mathrm{m}^{-1}$, well below the cutoff wavenumber of 0.2 m^{-1}. The fit parameters ($\hat{G}_0$ and $\hat{k}_{y0}$) will be nondimensionalized and scaled in Section 4.

c. Cross-shore and time-lagged correlation

We next examine the last term (C_{XT}) that makes up the covariance of the vorticity forcing C_G (7). Based on (7), the cross-shore-(Δx) and time- (Δt) lagged correlation of vorticity forcing C_{XT} is

$$C_{XT}(\Delta x, \Delta t; x) = \frac{\langle G_i(x,t)G_i(x+\Delta x, t+\Delta t)\rangle}{\langle G_i^2(x,t)\rangle^{1/2}\langle G_i^2(x+\Delta x, t+\Delta t)\rangle^{1/2}}, \tag{19}$$

where $\langle\cdot\rangle$ denotes averaging in time and alongshore. The averaging is done over 4801 s of 1 Hz time series and 12 different alongshore locations evenly spaced every 100 m. The statistics are not homogeneous in the cross-shore direction so only averaging in time and y is performed. The Δx and Δt resolution of C_{XT} is 1 m and 1 s respectively.

We first examine C_{XT} from a single simulation with $\beta = 0.02$, $H_{\mathrm{s}} = 1.1$ m, $T_{\mathrm{p}} = 14$ s, and $\sigma_\theta = 20°$ at 4 different surfzone locations ($x/L_{\mathrm{SZ}} = -0.625, -0.5, -0.375, -0.25$) in Fig. 6. In all cases, C_{XT} is essentially non-zero only along a diagonal band with magnitude that decays in Δx and Δt. The slope of the non-zero C_{XT} diagonal band is steeper farther offshore relative to onshore (Fig. 6) This slope is largely consistent with the shallow water phase speed $\sqrt{gh}$ where h is taken at $\Delta x = 0$ m

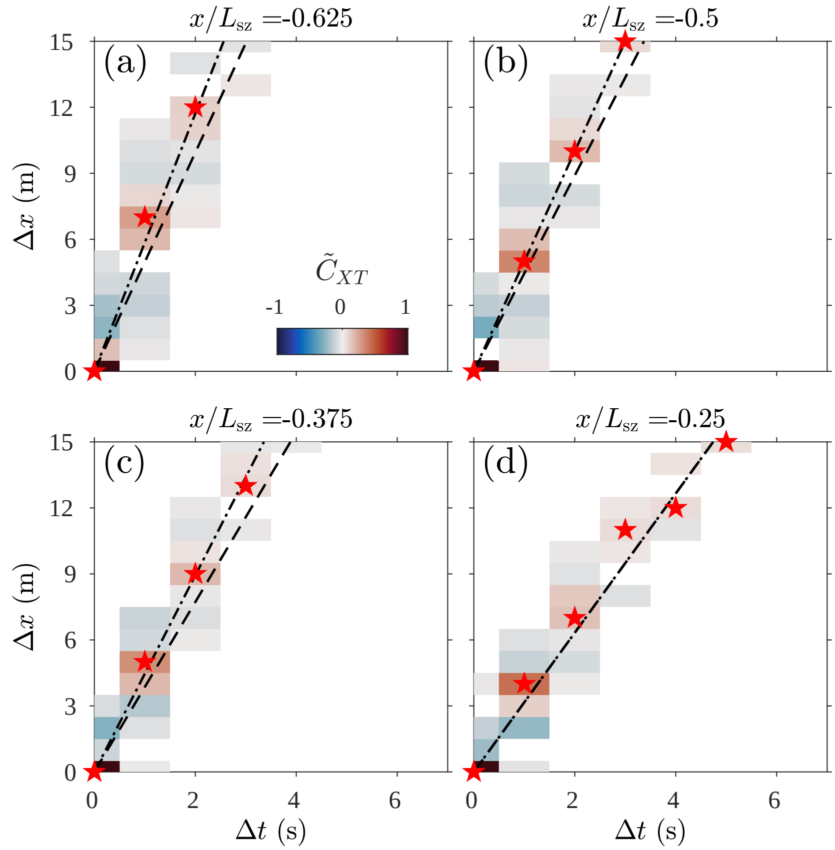

FIG. 6. Examples of cross-shore and time lagged correlation of the breaking-wave vorticity forcing C_{XT} (19) as a function of cross-shore lag (Δx) and time lag (Δt) at cross-shore locations (a) $x/L_{SZ} = -0.625$, (b) $x/L_{SZ} = -0.5$, (c) $x/L_{SZ} = -0.375$, and (d) $x/L_{SZ} = -0.25$ for a simulation with $\beta = 0.02$, $H_s = 1.1$ m, $T_p = 14$ s, and $\sigma_\theta = 20°$. Red star symbol indicates the maximum of C_{XT} at given Δt. Dashed line represents the characteristic of the shallow water phase velocity $\sqrt{gh}$ where h is taken to be at $\Delta x = 0$. Dash-dotted line represents the fitted velocity $\hat{c}$ from extracted maxima C_{XT} versus Δt (red star symbols). Note dashed line and dash-dotted line overlaps in (d). Blank space represents $|C_{XT}| < 0.02$ where it is statistically indistinguishable from 0 for a 95% confidence interval.

(dashed line in Fig. 6). Farther offshore C_{XT} decorrelates more rapidly in Δt (Fig. 6a), whereas closer to shore it decorrelates more slowly (Fig. 6d). For a fixed Δt, the non-zero C_{XT} band is wider in Δx farther offshore relative to onshore. This indicates larger Δx decorrelation scales in deeper water but larger Δt decorrelation scales in shallower water. In addition, for a fixed Δt, the sign of C_{XT} usually varies in Δx from positive on the peak of the diagonal to negative off-diagonal. This C_{XT} pattern is consistent with the vorticity forcing in relatively narrow cross-shore bands that

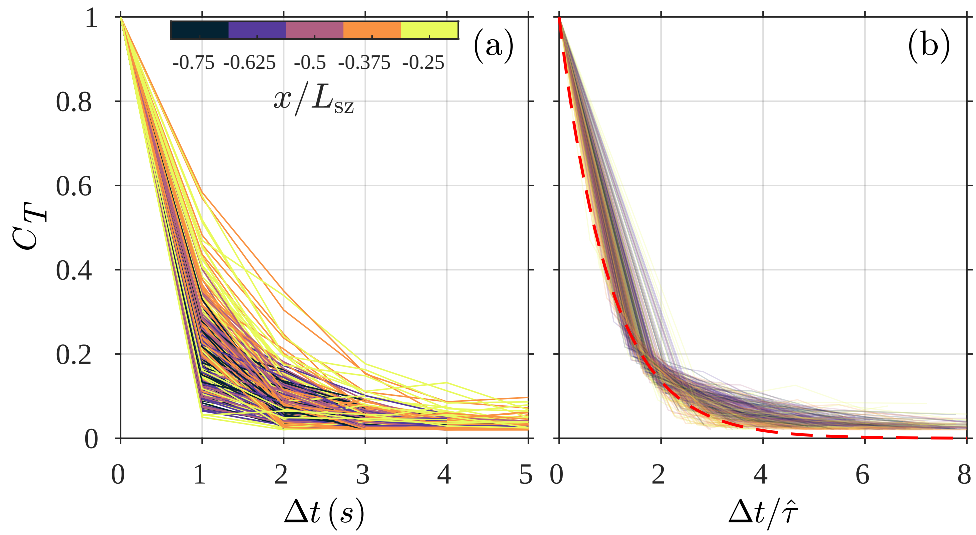

FIG. 7. (a) The diagonal component of lagged correlation C_T (21) versus time lag Δt. (b) C_T versus nondimensional time lag $(\Delta t/\hat{\tau})$, where $\hat{\tau}$ is the fit decorrelation time-scale and the red dashed line represents $\exp(-\Delta t/\hat{\tau})$. Both panels show five different surfzone locations for all 72 model simulations. The color legend in (a) indicates cross-shore locations x/L_{SZ}, where L_{SZ} is surfzone width.

propagate onshore at near the shallow water phase speed (Fig. 2). The $C_{XT}(\Delta x, \Delta t)$ structure for this example (Fig. 6) is consistent for all 72 simulations (not shown).

To compactly describe C_{XT}, we separate it into two functions

$$C_{XT}(\Delta x, \Delta t) = C_T(\Delta t) C_X(\Delta x - \hat{c}\Delta t), \tag{20}$$

where $\hat{c}$ is the slope of the diagonal-band, C_T is time-lagged correlation along the diagonal, *i.e.*, $C_T(\Delta t) = C_{XT}(c\Delta t, \Delta t)$, and C_X represents off-diagonal component of C_{XT}. This decomposition can be interpreted as crest-following C_T and cross-crest (C_X) correlations, respectively, the functional form of which will be derived from the simulations.

To extract the diagonal C_T, at each Δt we pick the local maximum $\Delta x_{\max}$ (red stars in Fig. 6) requiring that $|C_{XT}| > 0.02$ in order to avoid fitting to noise. This defined $C_T(\Delta t)$ as

$$C_T = C_{XT}(\Delta x_{\max}(\Delta t), \Delta t). \tag{21}$$

With the finite Δx resolution, uncertainty in the true $\Delta x_{\max}$ is present. We least-squares fit a line to $(\Delta x_{\max}, \Delta t)$ to obtain fit slope $\hat{c}$ (dash-dotted line in Fig. 6). We require at least three $\Delta x_{\max}(\Delta t)$ to estimate the slope. The $\Delta x_{\max}$ are nearly always located along the fit slope within the limits of the finite Δx resolution and the root-mean-square fit error (1.29 m) is near the Δx resolution. In the examples, $\hat{c}$ is close to the linear shallow water phase speed $\sqrt{gh}$ (compare dash-dotted and dashed lines in Fig. 6). The off-diagonal component of the cross-correlation becomes

$$C_X(\Delta x') = \frac{C_{XT}(\Delta x - \Delta x_{\max}(\Delta t), \Delta t)}{C_T(\Delta t)}. \tag{22}$$

However, for simplicity and to reduce fitting to noise, C_X is assumed to be independent of Δt, resulting in $C_X(\Delta x')$ where $\Delta x' = \Delta x - \Delta x_{\max}$. Thus $C_X(\Delta x' = 0) = 1$. We seek functional forms for $C_T(\Delta t)$ and $C_X(\Delta x')$ that are compactly represented by a few parameters. Using the definitions above, $\hat{c}$, C_T, and C_X are extracted from C_{XT} at 5 cross-shore locations ($x/L_{\mathrm{SZ}} = -0.75, -0.625, -0.5, -0.375, -0.25$) for all 72 simulations. Note C_X is extracted only at $\Delta t = 0$ s, *i.e.*, $C_X(\Delta x') = C_{XT}(\Delta x, \Delta t = 0)$.

For all simulations and cross-shore locations, the function $C_T(\Delta t)$ exhibits a decaying behavior, indicating rapid decorrelation, as the great majority of $C_T < 0.2$ for $\Delta t \geq 2$ s (Fig. 7a). At large Δt, C_T never decays fully to zero due requiring $|C_{XT}| > 0.02$ in defining $\Delta x_{\max}$. The decay time-scale is shorter for the outer surfzone relative to the inner-surfzone (colors in Fig. 7a). A simple decaying autocorrelation, consistent with a first-order autoregressive (AR1) stochastic process (Jenkins and Watts 1968), is

$$C_T(\Delta t) = \exp\left(-\Delta t/\hat{\tau}\right). \tag{23}$$

where $\hat{\tau}$ is the decorrelation time-scale. We fit C_T to (23) with the fit parameter $\hat{\tau}$. We require that the fit skill > 0.98, which rejects 3% of $\hat{\tau}$. The resulting C_T collapse when plotted against the non-dimensional time-scale $\Delta t/\hat{\tau}$ (Fig. 7b). This indicates that the extracted C_T are consistent with (23) and that $\hat{\tau}$ is well estimated (23). Overall, this suggests that the stochastic vorticity forcing following a wave crest can be represented by an AR1 process.

We next consider the off-diagonal component C_X (22). For all simulations and cross-shore locations, C_X decays rapidly (within 1–3 m) to a negative minimum between -0.2 to -0.5, often goes to a secondary positive maximum and eventually decays to near-zero (Fig. 8a). Although

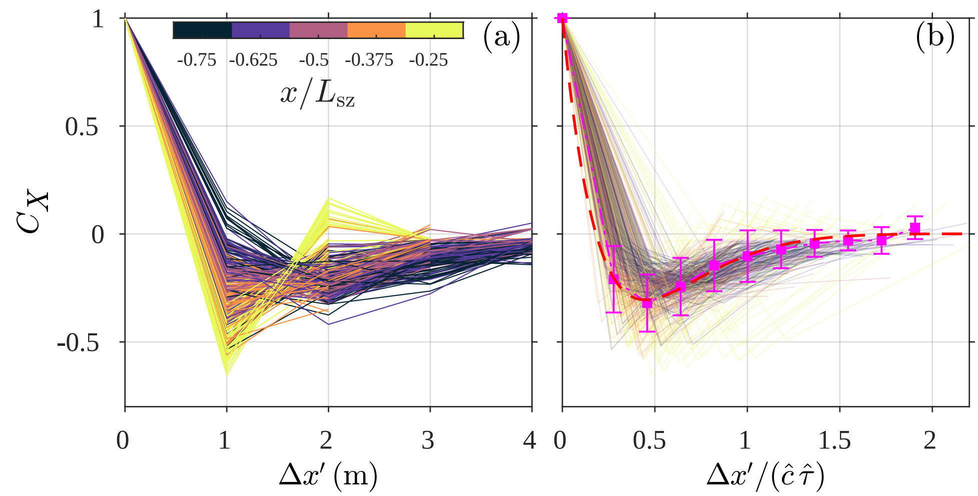

FIG. 8. (a) Off-diagonal C_X (22) at $\Delta t = 0$ versus cross-shore lag $\Delta x'$ at 5 different surfzone locations for all 72 model simulations. Color indicates cross-shore locations x/L_{SZ}, where L_{sz} is surfzone width. (b) C_X versus non-dimensional cross-shore lag $(\Delta x'/(\hat{c}\hat{\tau}))$ where $\hat{c}$ is the fit diagonal slope and $\hat{\tau}$ is the fit decorrelation time-scale in (23). Magenta error bar indicates binned-mean and $\pm$ standard deviation of C_X. Red dashed line indicates the fit function in (24).

the $\Delta x'$ resolution is poor, the decay is more rapid in shallower water closer to shore (yellow colors in Fig. 8). This sign switch suggests a coherent sign change of vorticity forcing across the breaking wave crest. As $\hat{\tau}$ represents the decorrelation time-scale and $\hat{c}$ the slope of the diagonal, a decorrelation length scale can be given $\hat{c}\hat{\tau}$. When plotted against the nondimensional $\Delta x'/(\hat{c}\hat{\tau})$, the C_X generally collapses over all cross-shore locations and simulations (Fig. 8b). The binned meaned C_X reveals the decaying and oscillatory pattern and the binned standard deviations (≈ 0.15, magenta in Fig. 8b) are generally much smaller than the variability of $C_X(\Delta x)$ (Fig. 8a). The binned mean $C_X(\Delta x'/(\hat{c}\hat{\tau}))$ can be fit to a decaying and oscillating function

$$C_X = \exp\left[-C_1 \Delta x'/(\hat{c}\hat{\tau})\right] \cos\left[C_2 \Delta x'/(\hat{c}\hat{\tau}) + C_3\right] / \cos\left(C_3\right), \tag{24}$$

where C_1, C_2, and C_3 are fit parameters with $C_1 = 3.57$, $C_2 = 1.82$, and $C_3 = 1.24$. By definition $C_X(\Delta x'/(\hat{c}\hat{\tau}) = 0) = 1$. The functional form (24) fits very well the binned means (compare dashed red and magenta squares in Fig. 8b). Here, we only calculate C_X for $\Delta x' \geq 0$, but as the C_X width is narrow relative to the cross-shore variation in the statistics, we expect (24) to be applicable for negative $\Delta x'$. These C_X results imply that no new parameter is needed to describe C_X. With the functional forms of C_T (23) and C_X (24) together with the fit diagonal slope $\hat{c}$ and decorrelation time-scale $\hat{\tau}$, the complete $C_{XT}(\Delta x, \Delta t)$ can be now be described.

4. Scaling the parameters describing the vorticity forcing covariance

We have extracted, for all simulations and at five cross-shore locations, the four dimensional parameters ($\hat{G}_0$, $\hat{k}_{y0}$, $\hat{c}$, and $\hat{\tau}$) that compactly describe components of the covariance C_G (6). We expect these parameters to depend parameterically upon x through model parameters such as beach slope β, water depth $h(x)$, or wave directional spread at the breakpoint $\sigma_{\theta b}$. The next step is to nondimensionalize each of these four parameters and scale them with non-dimensional parameters.

We first address the vorticity forcing standard deviation $\hat{G}_0$ (18). To establish a scaling for $\hat{G}_0$, we use the relationship between wave-averaged (*e.g.,* COAWST, DELFT3D) momentum forcing to mean wave-dissipation D_{w} and phase speed c, (*e.g.,* Smith 2006),

$$|\mathbf{F}_{\mathrm{br}}| = \frac{D_{\mathrm{w}}}{c}. \tag{25}$$

We estimate D_{w} from the cross-shore gradient of the model-estimated wave energy flux. Assuming shallow water wave conditions (*i.e.,* $c = \sqrt{gh}$) and considering that (25) is the depth-integrated force for the entire water-column, a general dimensional scale of depth-normalized breaking force (units $\mathrm{m\,s^{-2}}$) can be

$$\frac{D_{\mathrm{w}}}{(gh)^{1/2} h_b},$$

where h_b is the water depth at the breakpoint. We then use the $1/h_b$ as an inverse length scale to represent the derivative in the curl operator to arrive at a dimensional scale for vorticity forcing magnitude G_0, *i.e.,*

$$\hat{G}_0 \propto \frac{D_{\mathrm{w}}}{(gh)^{1/2} h_b^2}, \tag{26}$$

where D_{w} and h are functions of x. This implies that the ratio

$$\frac{\hat{G}_0 (gh)^{1/2} h_b^2}{D_w} \tag{27}$$

should only be a function of non-dimensional parameters. In fact, this ratio is largely a function of only beach slope β and wave directional spread at the breakpoint $\sigma_{\theta b}$, as shown below. First we define the nondimensional parameter,

$$\tilde{G}_0 := \frac{\hat{G}_0 (gh)^{1/2} h_b^2}{D_w} \beta. \tag{28}$$

This parameter $\tilde{G}_0$ is largely a linear function of $\sigma_{\theta b}$ and collapses ($r^2 = 0.68$) the variability of the vorticity forcing at all five x locations and over the 72 simulations (Fig. 9a). The best-fit linear scaling (red dashed line in Fig 9a) is

$$\tilde{G}_0 = 0.041 \sigma_{\theta b} + 0.059. \tag{29}$$

The largest deviations from a collapsed scaling occur closest to shore ($x/L_{\mathrm{SZ}} = -0.25$) and for the steepest slope ($\beta = 0.04$, yellow triangles in Fig. 9a). Other choices for nondimensional $\tilde{G}_0$ also have high skill. For example using (27) as $\tilde{G}_0$ results in squared correlation of $r^2 = 0.61$ (not shown). Clearly, the wave directional spread plays a significant role in the magnitude of the vorticity forcing.

We next examine the parameter $\hat{k}_{y0}$ representing the peak wavenumber of the vorticity forcing spectra (Section 3a). We have already seen that $\hat{k}_{y0}$ is larger in shallower water (Fig. 4a). Thus, we nondimensionalize the peak wavenumber with the local water depth $\hat{k}_{y0} h$, which should be a function of nondimensional parameters. We define a nondimensional $\tilde{k}_{y0}$ that includes the breaking Irribaren number $\mathrm{Ir_b}$ (4),

$$\tilde{k}_{y0} := \hat{k}_{y0}\, h\, \mathrm{Ir_b}. \tag{30}$$

The $\tilde{k}_{y0}$ is also a linear function of $\sigma_{\theta b}$ and collapses ($r^2 = 0.77$) the variability of k_y at all five x locations and over the 72 different simulations (Fig. 9b). The best fit linear scaling (red dashed line in Fig. 9) is

$$\tilde{k}_{y0} = 9.5 \times 10^{-4} \sigma_{\theta b} + 1.9 \times 10^{-3}. \tag{31}$$

Overall, the deviation from the scaling is positive for steepest slopes and negative for the shallowest slopes. As with vorticity forcing magnitude, the wave directional spread clearly plays a significant role in setting the alongshore length-scales of vorticity forcing.

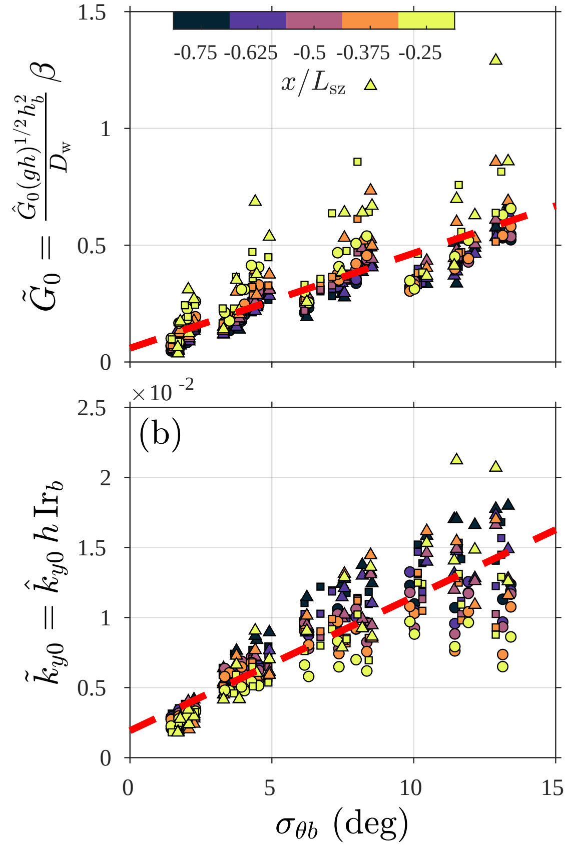

FIG. 9. (a) Non-dimensional breaking-wave vorticity forcing magnitude $\tilde{G}_0$ (28) and (b) non-dimensional peak alongshore wavenumber $\tilde{k}_{y0}$ (30) versus directional spread at break point $\sigma_{\theta b}$. h is local water depth, h_b water depth at break point, D_w local wave dissipation, and $\mathrm{Ir_b}$ Iribarren number evaluated at break point (4). Red dashed line indicates the best linear fit. Color indicates cross-shore locations $x/L_{\rm SZ}$, where $L_{\rm SZ}$ is surfzone width. Symbols indicates beach slope ($\beta = 0.02$, circle; $\beta = 0.03$, square; $\beta = 0.04$, triangle).

We next examine the C_{XT} fit diagonal slope $\hat{c}$. The dimensional slope $\hat{c}$ is linearly related with high correlation ($r^2 = 0.92$) and near-one slope to the linear shallow water phase speed $\sqrt{gh}$ (Fig. 10). This makes the statistical case for what was seen in Fig. 6, that the non-zero diagonal slope of C_{XT} is the result of onshore wave propagation. Generally $\hat{c}$ is slightly larger than $\sqrt{gh}$ and the deviations from a 1:1 relationship are largest at the most offshore location ($x/L_{\rm SZ} = -0.75$, dark symbol in Fig 10). Over all five cross-shore locations the binned mean $\hat{c}/\sqrt{gh}$ is largely consistent varying from 1.08 to 1.11. This value just greater than one is consistent with phase speed of a nonlinear shallow water wave. No $\hat{c}/\sqrt{gh}$ scaling that depended on other non-dimensional parameters was

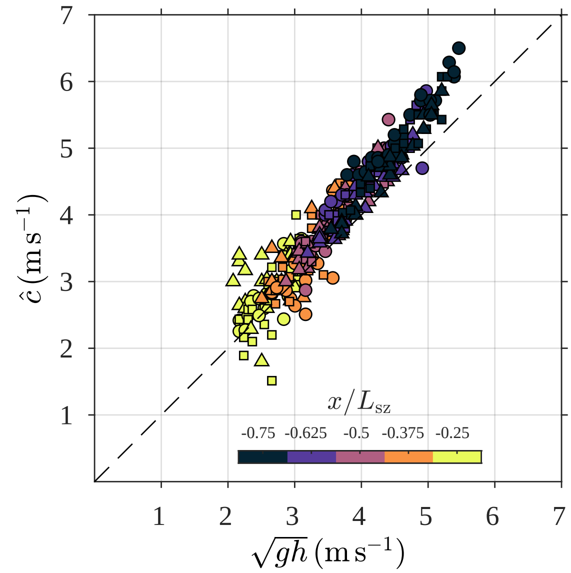

FIG. 10. The fit slope $\hat{c}$ of the non-zero diagonal of C_{XT} versus shallow water phase velocity $\sqrt{gh}$ at five different surfzone locations for all 72 simulations. Dashed represents a 1:1 relationship. Color indicates cross-shore locations x/L_{SZ}, where L_{SZ} is surfzone width. The squared correlation is $r^2 = 0.92$. Symbols indicates beach slope ($\beta = 0.02$, circle; $\beta = 0.03$, square; $\beta = 0.04$, triangle).

found that improved upon the dimensional scaling. Thus, here we use the dimensional scaling of

$$\frac{\hat{c}}{\sqrt{gh}} = 1.10. \tag{32}$$

The last dimensional parameter we examine is the forcing decorrelation time-scale $\hat{\tau}$. We nondimensionalize $\hat{\tau}$ with the time-scale $\sqrt{H_{\mathrm{sb}}/g}$,

$$\tilde{\tau} = \hat{\tau}\sqrt{g/H_{\mathrm{sb}}}, \tag{33}$$

where H_{sb} is the significant wave height at breaking. In the outer half of the surfzone ($x/L_{SZ} \le -0.5$), the binned-mean $\tilde{\tau}$ are largely uniform near 2 with standard deviations of 0.35 (Fig. 11a). In the inner-surfzone ($x/L_{SZ} > -0.5$), $\tilde{\tau}$ increases by 35% in the inner-surfzone, with standard deviation of 1.1. In general, longer decorrelation time-scales are associated with larger $\sigma_{\theta b}$ (lighter color in Fig. 11a). However, $\sigma_{\theta b}$ alone cannot scale $\tilde{\tau}$. Here, neither β nor $\mathrm{Ir_b}$ has skill in

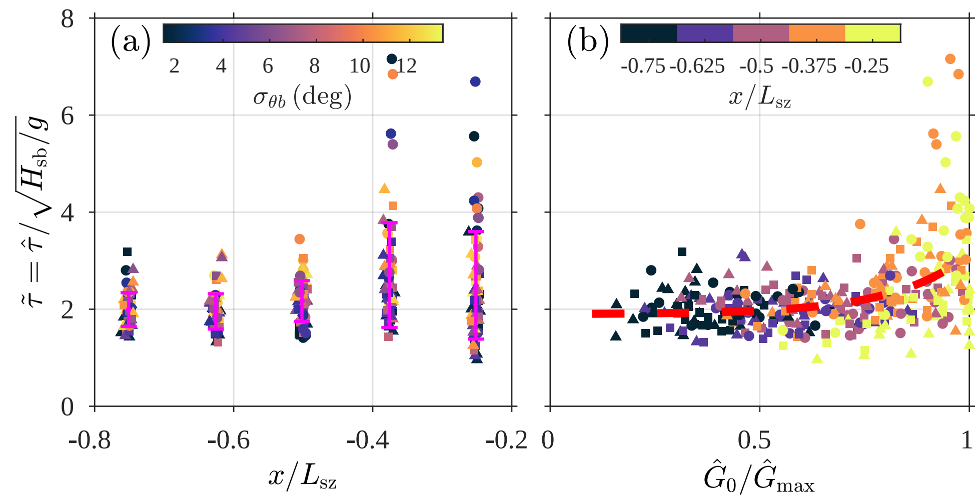

FIG. 11. (a) Non-dimensional decorrelation time-scale $\tilde{\tau}$ (33) versus non-dimensional cross-shore location (x/L_{SZ}), where L_{SZ} is surfzone width. Magenta error bar indicates binned-mean and ± standard deviation of $\tilde{\tau}$. Color legend indicates wave directional spread at breaking $\sigma_{\theta b}$. (b) Nondimensional $\tilde{\tau}$ versus non-dimensional forcing magnitude $\hat{G}_0/\hat{G}_{\max}$ at five surfzone locations (colors) and for all 72 simulations. The $\hat{G}_0$ is the forcing standard deviation at the location of $\hat{\tau}$ and $\hat{G}_{\max}$ is the cross-shore maximum of $\hat{G}_0$. Color indicates cross-shore locations x/L_{SZ}, where L_{SZ} is surfzone width. Symbols indicates beach slope ($\beta = 0.02$, circle; $\beta = 0.03$, square; $\beta = 0.04$, triangle).

scaling $\tilde{\tau}$. Nondimensionalizing $\hat{\tau}$ with peak wave period T_p also does not yield a good scaling. The cross-shore variation of $\tilde{\tau}$ resembles the cross-shore variation of forcing standard deviation (Fig. 3e,f), suggesting a scaling using $\hat{G}_0$. At all five cross-shore locations and simulations, $\tilde{\tau}$ largely collapses as a function of the normalized vorticity forcing magnitude $\hat{G}_0/\hat{G}_{\max}$ (Fig. 11b), where $\hat{G}_0$ is evaluated at the location where $\hat{\tau}$ is calculated and $\hat{G}_{\max}$ is the cross-shore maximum for that simulation (see Fig.3e,f). For $\hat{G}_0/\hat{G}_{\max} < 0.7$, the $\tilde{\tau}$ are largely near 2 with small variability. For larger $\hat{G}_0/\hat{G}_{\max}$, $\tilde{\tau}$ increases with increased variability. Here, the relationship between $\tilde{\tau}$ and $\hat{G}_0/\hat{G}_{\max}$ is represented with an exponential function

$$\tilde{\tau} = 4.6 \times 10^{-3} \exp\left(5.61\, \hat{G}_0/\hat{G}_{\max}\right) + 1.90. \tag{34}$$

This fit exponential (red dashed line in Fig. 11) begins to increase for the $x/L_{SZ} > -0.5$ matching the inner-surfzone increase of $\tilde{\tau}$. The skill of an exponential fit between $\tilde{\tau}$ and $\hat{G}_0/\hat{G}_{\max}$ is reasonable at $r^2 = 0.22$, but is reduced relative to the other scalings because at larger $\hat{G}_0/\hat{G}_{\max}$ the variability of $\tilde{\tau}$ is large. Lastly, we note that the off-diagonal C_X decays with $\Delta x'/(\hat{c}\hat{\tau})$. This implies that the cross-crest decay length-scale goes like $\sim \sqrt{gh(x)} \times \sqrt{H_{\rm sb}/g} = \sqrt{H_{\rm sb}h(x)}$, which is a few meters at most and gets shorter onshore.

5. Discussion

a. Recapitulation and relationship to prior work

We have described the vorticity forcing covariance C_G (6) in terms of separable functions governing its magnitude and alongshore, cross-shore, and time lagged structure across the surfzone. We have shown that the local vorticity forcing standard deviation $\hat{G}_0(x)$ is a function of local wave dissipation, water depth, beach slope, and wave directional spread at the breakpoint $\sigma_{\theta b}$ that varies from 2° to 13.5° (Fig. 9a). Thus, if these quantities are known across the surfzone then $\hat{G}_0(x)$ can be estimated, a first step to a potential parameterization. The $\tilde{G}_0$ increase with $\sigma_{\theta b}$ is consistent with the increase in surfzone averaged $\nabla \times \mathbf{F}_{\rm br}$ variance with wavemaker generated σ_θ from 0°, 10° and 20° (O'Dea et al. 2021). In contrast, in a modeling study of a laboratory barred-beach surfzone, the mean vorticity forcing magnitude $|\nabla \times \mathbf{F}_{\rm br}|$ averaged over all breaking crests increased with $\sigma_{\theta b}$ up to a maximum near 10° and decreased for larger $\sigma_{\theta b}$ (Nuss et al. 2025). This inconsistency could be due to several factors. First, perhaps our modeled $\sigma_{\theta b}$ is not large enough. Second, the Nuss et al. (2025) $|\nabla \times \mathbf{F}_{\rm br}|$ metric is only averaged over crests that have sufficiently long-enough lateral extent. As breaking crests would get shorter with larger $\sigma_{\theta b}$, there may be a bias as the shortest crests are the most numerous (Nuss et al. 2025). Third, the $|\nabla \times \mathbf{F}_{\rm br}|$ metric resembles a L1 norm whereas variance is a L2 norm. These norms do not necessarily vary in the same manner. Fourth, here, on a planar bathymetry the $G_0(x)$ profiles are largest in the mid- to inner-surfzone (Fig. 3e,f). As discussed by Nuss et al. (2025), their barred-beach configuration may result in different cross-shore structures of wave dissipation and other relevant parameters on the non-monotonic profile that may impact vorticity generation in ways not yet understood.

At a particular cross-shore location, the vorticity forcing spectra $S_{\nabla\times\mathbf{F}_{\rm br}}(k_y)$ wavenumber dependence is well described by a specific Weibull distribution depending upon the peak wavenumber k_{y0} (Fig. 4b). The structure of $S_{\nabla\times\mathbf{F}_{\rm br}}(k_y)$ is similar to previously estimated cross-surfzone averaged $S_{\nabla\times\mathbf{F}_{\rm br}}(k_y)$, revealing vorticity forcing over a broad range of k_y (Feddersen 2014; O'Dea et al. 2021). The nondimensional peak wavenumber $\tilde{k}_{y0}$ is also a specific linear function of $\sigma_{\theta b}$ (Fig. 9b), consistent with the increasing $S_{\nabla\times\mathbf{F}_{\mathrm{br}}}$ peak wavenumber in O'Dea et al. (2021). Nuss et al. (2025) examined alongshore variability through breaking-wave crest length λ_c and crest-end density d_{ce} statistics, which were consistent between the model and laboratory study of Baker et al. (2023). Mean λ_c decreased and d_{ce} increased with increasing $\sigma_{\theta b}$ which is consistent with shorter alongshore scales (increased k_{y0}) with $\sigma_{\theta b}$. The $\tilde{k}_{y0}$ scaling implies that with known $\mathrm{Ir_b}$ (4), $\sigma_{\theta b}$, $h(x)$, $\hat{k}_{y0}$ can be estimated, as can entire $S_Y(k_y)$.

At a particular x location, the cross- and time-lagged correlation C_{XT} is strongly diagonal (Fig. 6) and can be decomposed into diagonal $C_T(\Delta t)$ and offdiagonal $C_X(\Delta x - \hat{c}\Delta t)$ components. The slope of the diagonal is consistent with the shallow water phase speed (Fig. 10), implying - as expected - that the vorticity forcing propagates onshore with the wave crests. Scaling $\hat{c}$ with a nonlinear phase speed (*e.g.*, $\sqrt{g(h+H_{\mathrm{s}})}$) did not improve the fit. The $C_T(\Delta t)$ is well represented by an exponential decay with time-scale $\hat{\tau}$, consistent with an AR1 random process (Fig. 7). The $\hat{\tau}$ is short (mostly between 0.5–1.25 s) relative to the wave period, indicating rapid decorrelation. The nondimensional time-scale $\tilde{\tau} = \hat{\tau}\sqrt{g/H_{\mathrm{sb}}}$ can be scaled by $\hat{G}_0/\hat{G}_{\mathrm{max}}$ (Fig. 11). The off-diagonal portion of the covariance C_X is well represented by a decaying oscillating function (24) with the cross-shore decorrelation length-scale $\hat{c}\hat{\tau}$ (Fig. 8b), which is a few meters at most, much shorter that the separation between successive wave crests. The C_{XT} results suggest a parameterization with narrow cross-crest structure that get smaller in shallower depths, propagates onshore with $\sqrt{gh}$ and time-decorrelates with $\hat{\tau}$.

The cross-shore or temporal- structure of $\nabla\times\mathbf{F}_{\mathrm{br}}$ has not been previously examined. A clear feature of C_{XT} is the off-diagonal ($\Delta x'$) negative correlations. This indicates a consistent forcing sign switch across the wave crest, as seen in a blow up (Fig. 12) of the $\nabla\times\mathbf{F}_{\mathrm{br}}$ example shown in Fig. 2b. This outer-surfzone breaking crest spans about 30 m in the alongshore. At the center of the crest $\nabla\times\mathbf{F}_{\mathrm{br}}$ is relatively weak and is largest at the crest ends (Fig. 12). In between the crest center and end, alongshore bands of cross-shore alternating sign $\nabla\times\mathbf{F}_{\mathrm{br}}$ are evident. Such features are consistent across most breaking wave crests. Analogous cross-crest variation in $|\nabla\times\mathbf{F}_{\mathrm{br}}|$ is seen in Nuss et al. (2025). We qualitatively explain how this pattern occurs. The alongshore component

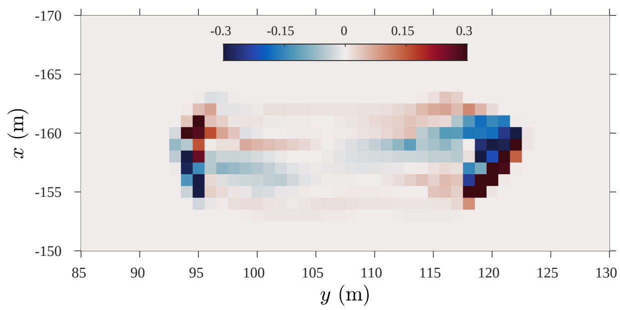

FIG. 12. Zoomed in view of the modeled breaking-wave vorticity forcing $\nabla \times \mathbf{F}_{\mathrm{br}}$ from the dashed box in Fig. 2b versus cross-shore (x) and alongshore (y) coordinates. Model parameters are beach slope $\beta = 0.02$ and incident wave parameters: $H_s = 1.1\,\mathrm{m}$, $T_p = 8\,\mathrm{s}$, and $\sigma_\theta = 20°$.

of $\mathbf{F}_{\mathrm{br}}$ has a term that goes like

$$(h+\eta)^{-1}\frac{\partial}{\partial x}\left(\nu_b \frac{\partial (h+\eta)v}{\partial x}\right), \tag{35}$$

where ν_b is the breaking eddy viscosity which is non-zero in the breaking wave crest. Right at the breaking wave crest, $\nabla \times \mathbf{F}_{\mathrm{br}}$ introduces a ∂_x in (35) resulting in terms like $\partial^3 v/\partial x^3$. This derivative will generate cross-shore sign changes around the maximum of v and η at the breaking wave crest.

b. Limitations

Here, we have described and scaled the second order statistic, *i.e.,* lagged covariance C_G, of the vorticity forcing. However, we have neglected third (skewness, asymmetry, or bispectra), fourth (kurtosis), or higher order statistics that may be important in describing the structure of $\nabla \times \mathbf{F}_{\mathrm{br}}$. For example, the $S_Y(k_y)$ doesn't capture any phase information. Breaking wave crests are alongshore coherent with their own particular statistics (*e.g.,* Baker et al. 2023; Nuss et al. 2025). These statistics are neglected with the focus on covariance. In the analysis of C_G, we have made a number of assumptions, including that C_G is separable (7), that $C_{XT}(\Delta x, \Delta t)$ is also a separable function of $C_T(\Delta t)$ and $C_X(\Delta x')$. Only on planar beaches has C_G been described and scaled and over a relatively limited range of beach slope and incident wave statistics spanning 72 simulations. Planar beach slope β is a key parameter for $\hat{G}_0$ and is also important, through Ir_{b}, for $\hat{k}_{y0}$. But outside of idealized situations, most beach profiles have variable slope. For monotonic beach profiles, presumably the local β can be used in the scalings. However, on non-monotonic (such as barred beach) profiles, β can be locally negative which is not permitted in the scalings for $\hat{G}_0$ (28) or $\hat{k}_{y0}$ (30). In contrast, parts of the modeled surfzone of Nuss et al. (2025) had negative local beach slope. This may also explain why the vorticity forcing magnitude relationship with $\sigma_{\theta b}$ is different betweeen our planar and their barred profiles. Lastly, we have only analyzed simulations with mean normally incident waves, *i.e.,* $\bar{\theta} = 0°$. For mean obliquely incident waves, the statistics of $\nabla \times \mathbf{F}_{\mathrm{br}}$ will change and at a minimum involve a new parameter of $\bar{\theta}$.

c. A pathway to parameterizing vorticity forcing in the surfzone

We conclude by sketching out a $\nabla \times \mathbf{F}_{\mathrm{br}}$ parameterization pathway with an alongshore uniform bathymetry utilizing the functional form and parameters of C_G (6). A $\nabla \times \mathbf{F}_{\mathrm{br}}$ parameterization would be useful as 3D nonhydrostatic models that resolve the surfzone such as CROCO (Treillou et al. 2025) are too computationally expensive to simulate large model domains. A parameterization should generate stochastic realizations of $\nabla \times \mathbf{F}_{\mathrm{br}}$ that have appropriate second order statistics such as variances, alongshore wavenumber spectra, and cross- and time-decorrelation scales. We take inspiration from the stochastic forcing of 2D turbulence models (*e.g.,* Maltrud and Vallis 1991; Srinivasan and Young 2014), where typically stochastic forcing is prescribed only by a stochastic amplitude with a time-scale forced on a specific wavelength. We take an analogous approach where the stochastic forcing results in a covariance matching C_G.

We write parameterized G as an inverse Fourier transform in k_y

$$\nabla \times \mathbf{F}_{\mathrm{br}} = G(x,y,t) = \frac{\hat{G}_0(x)}{2\pi} \int_{-\infty}^{\infty} a(k_y, x - \hat{c}t) \exp(\mathrm{i} k_y y)\, \mathrm{d}k_y, \tag{36}$$

where $\hat{G}_0(x)$ sets the vorticity forcing magnitude, and the amplitude $a(k_y, x - \hat{c}t)$ propagates onshore with speed $\hat{c}$. We can decompose these Fourier amplitudes into separable functions

$$a(k_y, x - \hat{c}t) = \tilde{a}(k_y; x) W(x - \hat{c}t) b(t),$$

where $\tilde{a}(k_y; x)$ represents the alongshore variability, the non-stochastic envelope function $W(x - \hat{c}t)$ represents the onshore propagating cross-shore structure of the vorticity forcing propagating at $\hat{c}(x) = 1.10\sqrt{gh(x)}$ (32), and $b(t)$ is a stochastic process representing variability moving with the breaking-wave crest. We ensure that this parameterized G (36) results in a C_G form of (7). Taking $\langle G(x,y,t)G(x+\Delta x, y+\Delta y, t+\Delta t)\rangle$ results in the parameterized covariance,

$$C_G = \hat{G}_0(x)\hat{G}_0(x+\Delta x)\underbrace{\left[\int |\tilde{a}(k_y)|^2 \exp(\mathrm{i}k_y\Delta y)\mathrm{d}k_y\right]}_{A}\underbrace{\langle [W(x-\hat{c}t)W(x+\Delta x-\hat{c}(t+\Delta t))b(t)b(t+\Delta t)]\rangle}_{B}, \tag{37}$$

where the angle brackets represent a phase average. This form matches that of (7), where A is $C_Y(\Delta y)$, and B is $C_{XT}(\Delta x, \Delta t)$. The two $\hat{G}_0$ terms go outside the $\langle\rangle$ operator as long as $\hat{G}_0(x)$ varies slowly relative to the cross-shore decorrelation length-scale $\hat{c}\hat{\tau}$. The magnitude of $\nabla\times\mathbf{F}_{\mathrm{br}}$ is set by the scaling of $\hat{G}_0(x)$ (28 & 29).

Now we choose the expressions $\tilde{a}(k_y;x)$, $W(x-\hat{c}t)$, and $b(t)$ so that the parameterized $C_Y(\Delta y)$ and $C_{XT}(\Delta x, \Delta t)$ match the derived functional forms. First we choose $\tilde{a}(k_y;x)$ with random phases from the Weibull spectral form with the peak wavenumber $\hat{k}_{y0}$ derived from the scaling (30 & 31) giving the implicit x dependence. To prevent very large $\hat{k}_{y0}$, we limit to $\hat{k}_{y0} = 0.15\ \mathrm{m}^{-1}$ at depths $h < 0.75$ m. The $\tilde{a}$ phases are set to be cross-shore uniform.

We next ensure that the parameterized C_{XT} has diagonal slope that matches $C_T(\Delta t)$ (23). We define $\theta = x-\hat{c}t$ for convenience. We can decompose B for $\theta = 0$ and $\Delta x - \hat{c}\Delta t = 0$, representing the diagonal portion of C_{XT} which by definition is $C_T(\Delta t)$. As $C_T(\Delta t = 0) = 1$, we require that both $\langle W(\theta)W(\theta)\rangle = 1$ and $\langle b(t)b(t)\rangle = 1$. Analogous to previous forced 2D turbulence studies (*e.g.,* Maltrud and Vallis 1991), we make $b(t)$ be a continuous AR1 stochastic process that evolves with unit variance, *i.e.,*

$$\frac{\mathrm{d}b}{\mathrm{d}t} = -\frac{b}{\hat{\tau}} + \sqrt{\frac{2}{\hat{\tau}}}\chi(t) \tag{38}$$

where $\hat{\tau}$ is the C_T-decorrelation time-scale and χ is a zero-mean, stationary, white noise process with variance $\langle\chi(t)\chi(t+\Delta t)\rangle = \delta(\Delta t)$. The $\hat{\tau}$ is derived from the scaling (33 & 34), where we use the scaled $\hat{G}_0$ (28 & 29) instead of G_0. The resulting $C_T = \langle b(t)b(t+\Delta t)\rangle = \exp(-t/\hat{\tau})$ by definition for an AR1 process (Jenkins and Watts 1968) and matches the derived $C_T(\Delta t)$ form (23).

Next, if we instead restrict B to $\Delta t = 0$, it becomes $C_X(\Delta x)$, allowing us to determine the functional form of $W(x-\hat{c}t)$. For $\Delta t = 0$, as a unit-variance AR1 process $\langle b^2(t)\rangle = 1$, and then $C_X = \langle W(\theta)W(\theta+\Delta x)\rangle$ where the average is now over θ from $-\Lambda/2$ to $\Lambda/2$, where Λ is the cross-shore separation between wave crests, scaling as $T_{\mathrm{p}}\sqrt{gh}$, which is ≈ 24 m for $T_{\mathrm{p}} = 8$ s and $h = 1$ m.

We choose the functional form for $W(\theta)$ to be

$$W(\theta) = \frac{A_1}{\cos A_4} \exp\left(-A_2 \frac{|\theta|}{\hat{c}\hat{\tau}}\right) \cos\left(A_3 \frac{|\theta|}{\hat{c}\hat{\tau}} + A_4\right) \tag{39}$$

with $A_1 = 3.16\sqrt{\Lambda/\hat{c}\hat{\tau}}$, $A_2 = 3.57$, $A_3 = 1.82$, and $A_4 = 1.10$. Representing the breaking wave region (Fig. 2b,c), W (39) is narrow. The crest separation scale is much larger than the W width ($\Lambda \gg \hat{c}\hat{\tau}$). As shown in Appendix B, with this form and parameters, C_X matches the derived functional form (24), *i.e.,*

$$\langle W(\theta)W(\theta+\Delta x)\rangle = \frac{1}{\Lambda}\int_{-\Lambda/2}^{\Lambda/2} W(\theta)W(\theta+\Delta x)\mathrm{d}\theta = \frac{\exp\left(-C_1\frac{\Delta x}{\hat{c}\hat{\tau}}\right)\cos\left(C_2\frac{\Delta x}{\hat{c}\hat{\tau}}+C_3\right)}{\cos(C_3)}, \tag{40}$$

where the θ-integration is a dummy for x integration. In practice, W repeats at the peak period T_p to represent a continuous train of wave crests and the crest separation Λ decreases in shallower water and is a function of T_p and $\hat{c}$, consistent with linear wave theory.

We demonstrate an example parameterization (Fig. 13) for a case with the same parameters as in the example in Fig. 2 with parameters $\beta = 0.02$, $H_\mathrm{sb} = 1.18$ m, $T_\mathrm{p} = 8\,\mathrm{s}$, $h_b = 3.44\,\mathrm{m}$, and $\sigma_{\theta b} = 13.13°$. For each wave $b(t)$ is calculated by numerically solving (38) with high temporal-resolution. The elements $\hat{G}_0(x)$, $\tilde{a}(k_y)$, $W(\theta)$ and $b(t)$ within (36) are combined to yield the $G(x,y,t) = \nabla\times\mathbf{F}_\mathrm{br}$. An example snapshot (Fig. 13) is qualitatively consistent with the WR-extracted $\nabla\times\mathbf{F}_\mathrm{br}$ (Fig. 2b,c). The parameterized forcing is in narrow alongshore-bands that propagate onshore and get narrower in shallow water, similar to the model (Fig. 2b). The alongshore variability is mostly at 10-30 m length-scales that get shorter in shallower water and there is a consistent cross-crest sign change, also similar to the model (Fig. 2c). However, there are distinct differences, the most important of which is that we no longer have alongshore coherent breaking-wave crests. A second difference is that our forcing bands occur every T_p, whereas in the model they are more random. Whether these differences would result in different vorticity distributions in the surfzone is unknown.

To use such a parameterization, the rotational forcing $\mathbf{F}_\mathrm{br}^\mathrm{(rot)}$ is estimated by solving for the forcing streamfunction $\nabla^2\psi_F = \nabla\times\mathbf{F}_\mathrm{br}$ and then $\mathbf{F}_\mathrm{br}^\mathrm{(rot)} = \nabla\times\psi_F$. This $\mathbf{F}_\mathrm{br}^\mathrm{(rot)}$ would be vertically distributed as surface intensified body force as for wave-averaged forcing (Kumar et al. 2012). A parameteri-

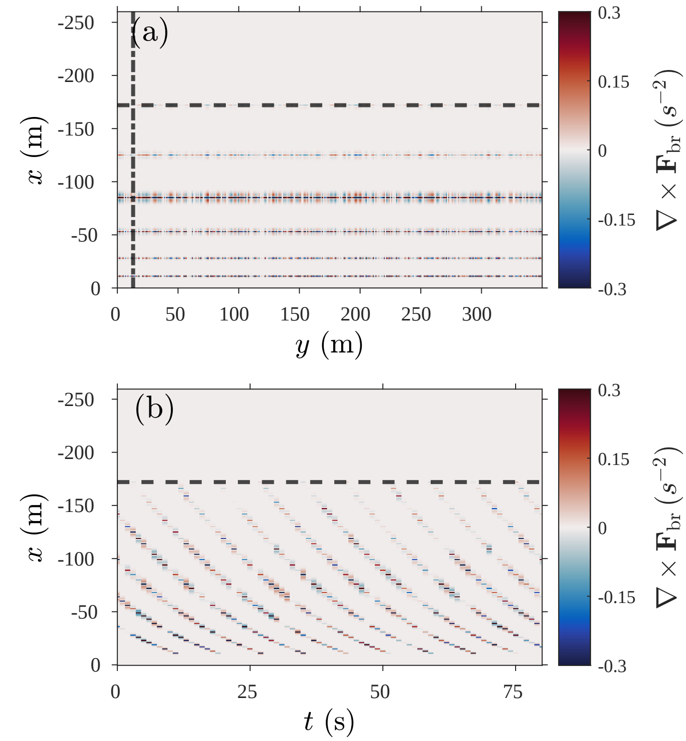

FIG. 13. Schematic example of the stochastic spectral parameterization $G(x,y,t) = \nabla \times \mathbf{F}_{\mathrm{br}}$ via (36): (a) snapshot of the parameterized breaking-wave vorticity forcing ($\nabla \times \mathbf{F}_{\mathrm{br}}$) versus cross-shore ($x$) and alongshore ($y$) coordinates. (b) Hovmöller diagram of parameterized $\nabla \times \mathbf{F}_{\mathrm{br}}$ as a function of cross-shore (x) and time (t) at the cross-shore transect shown in vertical black dash-dotted line in panel a. The horizontal black dashed line indicates the outer limit of the surfzone $x = -L_{\mathrm{SZ}}$, where $L_{\mathrm{SZ}} = 172$ m.

zation could be evaluated by comparing WR-model and WA-model with parameterization vorticity statistics across the surfzone and inner-shelf, as was done for one-way coupling (Kumar and Feddersen 2017a). As WR-models generate appropriate surfzone eddy (vorticity) fields (Feddersen et al. 2011; Clark et al. 2011; Hally-Rosendahl and Feddersen 2016), WA-models with a validated parameterization would also do so (Kumar and Feddersen 2017a). Such a parameterization would enable broad study of the interacting rip current and inner-shelf processes over larger regions and longer time-scales than presently possible.

Acknowledgments. This work is dedicated to the memory of Nirnimesh Kumar who many years ago inspired this work. This study was funded by the U.S. Army Corps of Engineers (W912HZ1920020 and W912HZ-24-2-0035). Initial efforts on this project were supported by the

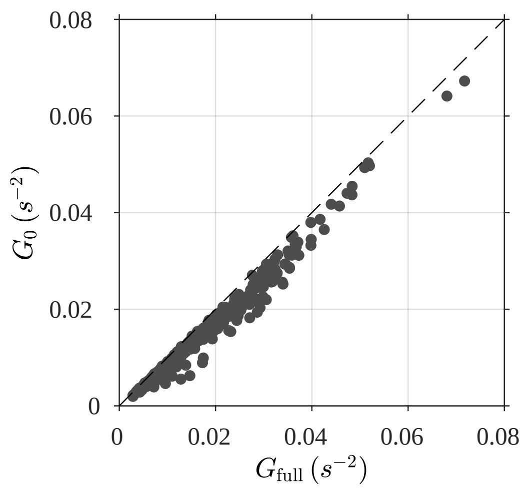

FIG. A1. Comparison of breaking-wave vorticity forcing magnitudes: G_0 (A1) versus G_{full} (A2). The dashed line represents the 1:1 relationship and the squared correlation between G_0 and G_{full} is $r^2 = 0.98$. The root-mean-square error between G_0 and G_{full} is 0.0032 s^{-2}.

Office of Naval Research under grant N00014-14-1-0553. SHS acknowledges support from the National Science Foundation awards OCE-1521653 and OCE-1735460.

Data availability statement. All the MATLAB data processing and plotting code is available at the Zenodo dataset repository and will be published upon acceptance.

APPENDIX A

The effect of neglecting high wavenumbers in estimating G_0

We are interested in forcing length-scales greater than the water depth which force 2D turbulence. As the model surfzone depths can be $h = 2.5$ m, our interest corresponds to wavenumbers up to $k_y = 0.2\ \mathrm{m}^{-1}$, corresponding to 5 m length-scales. Here, we examine the effect of neglecting wavenumbers above $k_y = 0.2\,\mathrm{m}^{-1}$ on G_0 by comparing the vorticity forcing magnitude G_0 calculated by integrating $S_{\nabla\times\mathbf{F}_{\mathrm{br}}}$ only up to $k_y = 0.2\ \mathrm{m}^{-1}$,

$$G_0 = \sqrt{\int_{0.0017\,\mathrm{m}^{-1}}^{0.2\,\mathrm{m}^{-1}} S_{\nabla\times\mathbf{F}_{\mathrm{br}}}\,\mathrm{d}k_y}\ , \tag{A1}$$

to that over all wavenumbers

$$G_{\text{full}} = \sqrt{\int_{0.0017\,\text{m}^{-1}}^{0.5\,\text{m}^{-1}} S_{\nabla\times\mathbf{F}_{\text{br}}}\, \mathrm{d}k_y} \,. \tag{A2}$$

The G_0 neglecting high wavenumbers (A1) is slightly smaller than but is highly correlated ($r^2 = 0.98$) with the full vorticity magnitude G_{full} (Fig. A1). The root-mean-square error is small ($0.0032\ \text{s}^{-2}$) relative to the variance of G_{full}. Thus, the variance at $k_y > 0.2\ \text{m}^{-1}$ is small and G_0 is representative of the vorticity forcing standard deviation.

APPENDIX B

The breaking wave vorticity forcing width function and relationship to C_X

We demonstrate the lagged-covariance of a single width envelope function $W(\theta)$ in the domain from $-\Lambda/2$ to $\Lambda/2$, where Λ is the separation between wave crests. We assume that $\Lambda \gg \hat{c}\hat{\tau}$. Let the functional form for $W(\theta)$ be

$$W(\theta) = \frac{A_1}{\cos A_4} \exp\left(-A_2 \frac{|\theta|}{\hat{c}\hat{\tau}}\right) \cos\left(A_3 \frac{|\theta|}{\hat{c}\hat{\tau}} + A_4\right) \tag{B1}$$

With (B1), we have

$$\begin{aligned}
\langle W(\theta) W(\theta+\Delta x)\rangle &= \frac{1}{\Lambda}\int_{-\Lambda/2}^{\Lambda/2} \frac{A_1^2}{\cos^2 A_4} \exp\left(-A_2 \frac{|\theta|}{\hat{c}\hat{\tau}}\right) \cos\left(A_3 \frac{|\theta|}{\hat{c}\hat{\tau}} + A_4\right) \exp\left(-A_2 \left(\frac{|\theta|}{\hat{c}\hat{\tau}} + \frac{\Delta x}{\hat{c}\hat{\tau}}\right)\right) \\
&\quad \times \cos\left(A_3 \left(\frac{|\theta|}{\hat{c}\hat{\tau}} + \frac{\Delta x}{\hat{c}\hat{\tau}}\right) + A_4\right) \mathrm{d}\theta \\
&= \frac{\hat{c}\hat{\tau}\, A_1^2}{\Lambda \cos^2 A_4} \exp\left(-A_2 \frac{\Delta x}{\hat{c}\hat{\tau}}\right) \left(B_1 \cos\left(A_3 \frac{\Delta x}{\hat{c}\hat{\tau}} + A_4\right) - B_2 \sin\left(A_3 \frac{\Delta x}{\hat{c}\hat{\tau}} + A_4\right)\right) \\
&= \frac{\hat{c}\hat{\tau}\, A_1^2 \sqrt{B_1^2 + B_2^2}}{\Lambda \cos^2 A_4} \exp\left(-A_2 \frac{\Delta x}{\hat{c}\hat{\tau}}\right) \cos\left(A_3 \frac{\Delta x}{\hat{c}\hat{\tau}} + \arctan(B_2/B_1) + A_4\right),
\end{aligned} \tag{B2}$$

where

$$B_1 = \int_{-\Lambda/2}^{\Lambda/2} \exp(-2A_2\hat{\theta})\cos(A_3\hat{\theta}+A4)\cos(A_3\hat{\theta})d\hat{\theta}, \tag{B3}$$

$$B_2 = \int_{-\Lambda/2}^{\Lambda/2} \exp(-2A_2\hat{\theta})\cos(A_3\hat{\theta}+A4)\sin(A_3\hat{\theta})d\hat{\theta}, \tag{B4}$$

where $\hat{\theta} = \frac{|\theta|}{\hat{c}\hat{\tau}}$ is the dummy variable for integration. To calculate the free parameters (A_1, A_2, A_3, A_4), we note that $\langle W(\theta)W(\theta+\Delta x)\rangle = C_X(\Delta x)$. Therefore

$$\begin{aligned}\langle W(\theta)W(\theta+\Delta x)\rangle &= \frac{\hat{c}\hat{\tau}\,A_1^2\sqrt{B_1^2+B_2^2}}{\Lambda\cos^2 A_4}\exp\left(-A_2\frac{\Delta x}{\hat{c}\hat{\tau}}\right)\cos\left(A_3\frac{\Delta x}{\hat{c}\hat{\tau}}+\arctan(B_2/B_1)+A_4\right)\\ &= \frac{1}{\cos(C_3)}\exp\left(-C_1\frac{\Delta x}{\hat{c}\hat{\tau}}\right)\cos\left(C_2\frac{\Delta x}{\hat{c}\hat{\tau}}+C_3\right).\end{aligned} \tag{B5}$$

Matching the coefficients yields

$$A_1 = \frac{\sqrt{\Lambda}\cos A_4}{\sqrt{\hat{c}\,\hat{\tau}\cos C_3}(B_1^2+B_2^2)^{1/4}} \tag{B6}$$

$$A_2 = C_1 \tag{B7}$$

$$A_3 = C_2 \tag{B8}$$

$$A_4 + \arctan(B_2/B_1) = C_3. \tag{B9}$$

Note with (B6) and (B9), $\langle W(\theta)W(\theta+\Delta x)\rangle$ $(\Delta x = 0) = C_X(\Delta x = 0) = 1$. Solving (B6) - (B9) results

$$A_1 = 3.16\sqrt{\Lambda/\hat{c}\hat{\tau}} \tag{B10}$$

$$A_2 = 3.57 \tag{B11}$$

$$A_3 = 1.82 \tag{B12}$$

$$A_4 = 1.10. \tag{B13}$$

References

Baker, C. M., M. Moulton, M. L. Palmsten, K. Brodie, E. Nuss, and C. C. Chickadel, 2023: Remotely sensed short-crested breaking waves in a laboratory directional wave basin. *Coastal*

Engineering, **183**, 104327.

Baker, C. M., M. Moulton, B. Raubenheimer, S. Elgar, and N. Kumar, 2021: Modeled three-dimensional currents and eddies on an alongshore-variable barred beach. *Journal of Geophysical Research: Oceans*, **126**, e2020JC016899.

Boehm, A. B., N. S. Ismail, L. M. Sassoubre, and E. A. Andruszkiewicz, 2015: Oceans in peril: Grand challenges in applied water quality research for the 21st century. *Environmental Engineering Science*.

Chen, Q., J. T. Kirby, R. A. Dalrymple, S. Fengyan, and E. B. Thornton, 2003: Boussinesq modeling of longshore currents. *J. Geophys. Res.*, **108**, doi: 10.1029/2002JC001308.

Chen, Q. H., R. A. Dalrymple, J. T. Kirby, A. B. Kennedy, and M. C. Haller, 1999: Boussinesq modeling of a rip current system. *J. Geophys. Res.*, **104**, 20617–20637.

Clark, D. B., S. Elgar, and B. Raubenheimer, 2012: Vorticity generation by short-crested wave breaking. *Geophys. Res. Lett.*, **39**, doi:10.1028/2012GL054034.

Clark, D. B., F. Feddersen, and R. T. Guza, 2010: Cross-shore surfzone tracer dispersion in an alongshore current. *J. Geophys. Res.*, **115**, doi:10.1029/2009JC005683.

— 2011: Modeling surfzone tracer plumes: 2. transport and dispersion. *J. Geophys. Res.*, **116**, doi:10.1029/2011JC007211.

Dooley, C., S. Elgar, and B. Raubenheimer, 2024: Field observations of surfzone vorticity. *Geophysical Research Letters*, **51**, e2024GL111402.

Elgar, S., C. Dooley, L. Gorrell, and B. Raubenheimer, 2023: Observations of two-dimensional turbulence in the surfzone. *Physics of Fluids*, **35**.

Elgar, S., and B. Raubenheimer, 2020: Field evidence of inverse energy cascades in the surfzone. *Journal of Physical Oceanography*, **50**, 2315–2321.

Feddersen, F., 2014: The generation of surfzone eddies in a strong alongshore current. *J. Phys. Ocean.*, **44**, doi:10.1175/JPO-D-13-051.1, 600–617.

Feddersen, F., A. B. Boehm, S. N. Giddings, X. Wu, and D. Liden, 2021: Modeling untreated wastewater evolution and swimmer illness for four wastewater infrastructure scenarios in the san diego-tijuana (us/mx) border region. *GeoHealth*, doi:10.1029/2021GH000490.

Feddersen, F., D. B. Clark, and R. T. Guza, 2011: Modeling of surfzone tracer plumes: 1. Waves, mean currents, and low-frequency eddies. *J. Geophys. Res.*, **116**, doi:10.1029/2011JC007210.

Grimes, D. J., and F. Feddersen, 2021: The self-similar stratified inner-shelf response to transient rip-current induced mixing. *J. Fluid Mech.*, doi:10.1017/jfm.2021.140.

Grimes, D. J., F. Feddersen, and N. Kumar, 2020: Tracer exchange across the stratified inner-shelf driven by transient rip-currents and diurnal surface heat fluxes. *Geophysical Research Letters*, **47**, doi:10.1029/2019GL086501, e2019GL086501.

Guza, R. T., and F. Feddersen, 2012: Effect of wave frequency and directional spread on shoreline runup. *Geophys. Res. Lett.*, **39**, doi:10.1029/2012GL051959.

Hally-Rosendahl, K., and F. Feddersen, 2016: Modeling surfzone to inner-shelf tracer exchange. *Journal of Geophysical Research: Oceans*, **121**, doi:10.1002/2015JC011530, 4007–4025.

Hally-Rosendahl, K., F. Feddersen, D. B. Clark, and R. T. Guza, 2015: Surfzone to inner-shelf exchange estimated from dye tracer balances. *Journal of Geophysical Research: Oceans*, doi:10.1002/2015JC010844, n/a–n/a.

Horwitz, R., and S. J. Lentz, 2014: Inner-Shelf Response to Cross-Shelf Wind Stress: The Importance of the Cross-Shelf Density Gradient in an Idealized Numerical Model and Field Observations. *Journal of Physical Oceanography*, **44**, doi:10.1175/JPO-D-13-075.1, 86–103.

Jenkins, G. M., and D. G. Watts, 1968: Spectral analysis and its applications. *Holden-Day, Inc., San Francisco, Card Nr. 67-13840.*

Johnson, D., and C. Pattiaratchi, 2006: Boussinesq modelling of transient rip currents. *Coastal Engineering*, **53**, doi:10.1016/j.coastaleng.2005.11.005, 419–439.

Kennedy, A. B., Q. H. Chen, J. T. Kirby, and R. A. Dalrymple, 2000: Boussinesq modeling of wave transformation, breaking and runup I: One dimension. *J. Waterway, Port, Coastal, and Ocean Eng.*, **126**, 39–47.

Kuik, A. J., G. P. V. Vledder, and L. H. Holthuijsen, 1988: A method for the routine analysis of pitch-and-roll buoy wave data. *J. Phys. Ocean.*, **18**, 1020–1034.

Kumar, N., and F. Feddersen, 2017a: The effect of stokes drift and transient rip currents on the inner shelf. part i: No stratification. *Journal of Physical Oceanography*, **47**, doi:10.1175/JPO-D-16-0076.1, 227–241.

— 2017b: The effect of stokes drift and transient rip currents on the inner shelf. part ii: With stratification. *Journal of Physical Oceanography*, **47**, doi:10.1175/JPO-D-16-0077.1, 243–260.

— 2017c: A new offshore transport mechanism for shoreline-released tracer induced by transient rip currents and stratification. *Geophysical Research Letters*, **44**, doi:10.1002/2017GL072611, 2843–2851, 2017GL072611.

Kumar, N., F. Feddersen, Y. Uchiyama, J. McWilliams, and W. O'Reilly, 2015: Midshelf to surfzone coupled ROMS-SWAN model data comparison of waves, currents, and temperature: Diagnosis of subtidal forcings and response. *J. Phys. Ocean.*, doi:10.1175/JPO-D-14-0151.1.

Kumar, N., G. Voulgaris, and J. C. Warner, 2011: Implementation and modification of a three-dimensional radiation stress formulation for surf zone and rip-current applications. *Coastal Eng.*, **58**, doi:10.1016/j.coastaleng.2011.06.009, 1097–1117.

Kumar, N., G. Voulgaris, J. C. Warner, and M. Olabarrieta, 2012: Implementation of the vortex force formalism in the coupled ocean-atmosphere-wave-sediment transport (COAWST) modeling system for inner shelf and surf zone applications. *Ocean Modelling*, **47**, doi:10.1016/j.ocemod.2012.01.003, 65 – 95.

Lentz, S. J., M. Fewings, P. Howd, J. Fredericks, and K. Hathaway, 2008: Observations and a model of undertow over the inner continental shelf. *J. Phys. Ocean.*, **38**, doi:10.1175/2008JPO3986.1, 2341–2357.

Lentz, S. J., and M. R. Fewings, 2012: The wind- and wave-driven inner-shelf circulation. *Annual Review of Marine Science*, **4**, doi:10.1146/annurev-marine-120709-142745, 317–343.

Lynett, P., 2006: Nearshore modeling using high-order boussinesq equations. *J. Waterway, Port, Coastal, and Ocean Engineering*, **132**, 348–357.

Maltrud, M. E., and G. K. Vallis, 1991: Energy spectra and coherent structures in forced two-dimensional and beta-plane turbulence. *Journal of Fluid Mechanics*, **228**, doi:10.1017/S0022112091002720, 321–342.

Marchesiello, P., F. Auclair, L. Debreu, J. McWilliams, R. Almar, R. Benshila, and F. Dumas, 2021: Tridimensional nonhydrostatic transient rip currents in a wave-resolving model. *Ocean Modelling*, **163**, 101816.

Masselink, G., M. Austin, J. Tinker, T. O'Hare, and P. Russell, 2008: Cross-shore sediment transport and morphological response on a macrotidal beach with intertidal bar morphology, truc vert, france. *Marine Geology*, **251**, 141–155.

Morgan, S. G., A. L. Shanks, J. H. MacMahan, A. J. Reniers, and F. Feddersen, 2018: Planktonic subsidies to surf-zone and intertidal communities. *Annual Review of Marine Science*, **10**, doi:10.1146/annurev-marine-010816-060514, 345–369, pMID: 28846492.

Nuss, E. S., M. Moulton, S. H. Suanda, and C. M. Baker, 2025: Modeled surf-zone eddies on a laboratory scale barred beach with varying wave conditions. *Journal of Geophysical Research: Oceans*, **130**, e2023JC020549.

Nwogu, O., 1993: Alternative form of Boussinesq equations for nearshore wave propagation. *J. Wtrwy., Port, Coast., and Oc. Engrg.*, **119**, 618–638.

O'Dea, A., N. Kumar, and M. C. Haller, 2021: Simulations of the surf zone eddy field and cross-shore exchange on a nonidealized bathymetry. *Journal of Geophysical Research: Oceans*, **126**, e2020JC016619.

Olabarrieta, M., J. C. Warner, and C. A. Hegermiller, 2023: Development and application of an infragravity wave (inwave) driver to simulate nearshore processes. *Journal of Advances in Modeling Earth Systems*, **15**, e2022MS003205.

Peregrine, D. H., 1998: Surf zone currents. *Theoretical and Computational Fluid Dynamics*, **10**, 295–309.

Pierson, W., and L. Moskowitz, 1964: Proposed spectral form for fully developed wind seas based on similarity theory of S A Kitaigorodskii. *J. Geophys. Res.*, **69**, doi:10.1029/JZ069i024p05181, 5181–5190.

Smith, J. A., 2006: Wave-current interactions in finite depth. *J. Phys. Ocean.*, **36**, doi:10.1175/JPO2911.1, 1403–1419.

Spydell, M., and F. Feddersen, 2009: Lagrangian drifter dispersion in the surf zone: Directionally spread, normally incident waves. *Journal of Physical Oceanography*, **39**, doi:10.1175/2008JPO3892.1, 809–830.

Spydell, M. S., F. Feddersen, R. T. Guza, and W. E. Schmidt, 2007: Observing surfzone dispersion with drifters. *J. Phys. Ocean.*, **27**, 2920–2939.

Srinivasan, K., and W. R. Young, 2014: Reynolds stress and eddy diffusivity of beta-plane shear flows. *Journal of the Atmospheric Sciences*, **71**, doi:10.1175/jas-d-13-0246.1, 2169–2185, n/a.

Suanda, S., S. Perez, and F. Feddersen, 2016: Evaluation of a source-function wavemaker for generating random directionally spread waves in the sea-swell band. *Coastal Engineering*, **114**, doi:10.1016/j.coastaleng.2016.04.006, 220–232.

Suanda, S. H., and F. Feddersen, 2015: A self-similar scaling for cross-shelf exchange driven by transient rip currents. *Geophysical Research Letters*, **42**, doi:10.1002/2015GL063944, 5427–5434, 2015GL063944.

Treillou, S., P. Marchesiello, C. M. Baker, J. McWilliams, and F. Dumas, 2025: Tracer dispersion by surfzone eddies: assessing the impact of undertow vertical shear. *Journal of Physical Oceanography*.

Uchiyama, Y., J. C. McWilliams, and C. Akan, 2017: Three-dimensional transient rip currents: Bathymetric excitation of low-frequency intrinsic variability. *Journal of Geophysical Research: Oceans*, **122**, 5826–5849.

Wei, Z., R. A. Dalrymple, M. Xu, R. Garnier, and M. Derakhti, 2017: Short-crested waves in the surf zone. *Journal of Geophysical Research: Oceans*, **122**, doi:10.1002/2016JC012485, 4143–4162.

Wu, X., F. Feddersen, and S. N. Giddings, 2021: Diagnosing surfzone impacts on inner-shelf flow spatial variability using realistic model experiments with and without surface gravity waves. *Journal of Physical Oceanography*, doi:10.1175/JPO-D-20-0324.

Wu, X., F. Feddersen, S. N. Giddings, N. Kumar, and G. Gopalakrishnan, 2020: Mechanisms of Mid- to Outer-Shelf Transport of Shoreline-Released Tracers. *Journal of Physical Oceanography*, **50**, doi:10.1175/JPO-D-19-0225.1, 1813–1837.